

# Substructure around M31 : Evolution and Effects

Jean-René Gauthier,<sup>1,3</sup> John Dubinski<sup>1</sup> and Lawrence M. Widrow<sup>2</sup>

## ABSTRACT

We investigate the evolution of a population of 100 dark matter satellites orbiting in the gravitational potential of a realistic model of M31. We find that after 10 Gyr, seven subhalos are completely disrupted by the tidal field of the host galaxy. The remaining satellites suffer heavy mass loss and overall, 75% of the mass initially in the subhalo system is tidally stripped. Not surprisingly, satellites with pericentric radius less than 30 kpc suffer the greatest stripping and leave a complex structure of tails and streams of debris around the host galaxy. Assuming that the most bound particles in each subhalo are kinematic tracers of stars, we find that the halo stellar population resulting from the tidal debris follows an  $r^{-3.5}$  density profile at large radii. We construct B-band photometric maps of stars coming from disrupted satellites and find conspicuous features similar both in morphology and brightness to the observed Giant Stream around Andromeda. An assumed star formation efficiency of 5-10% in the simulated satellite galaxies results in good agreement with the number of M31 satellites, the V-band surface brightness distribution, and the brightness of the Giant Stream. During the first 5 Gyr, the bombardment of the satellites heats and thickens the disk by a small amount. At about 5 Gyr, satellite interactions induce the formation of a strong bar which, in turn, leads to a significant increase in the velocity dispersion of the disk.

*Subject headings:* galaxies: interaction — methods: N-body simulations — cosmology : miscellaneous

## 1. Introduction

In the current cosmological paradigm, large-scale structure forms via hierarchical clustering wherein small systems composed of dark matter and gas merge to form larger objects.

---

<sup>1</sup>Department of Astronomy & Astrophysics, University of Toronto, Toronto, Canada

<sup>2</sup>Department of Physics and Astronomy, Queen's University, Kingston, Canada

<sup>3</sup>Email : gauthier@astro.utoronto.ca (JRG); dubinski@cita.utoronto.ca (JD); widrow@astro.queensu.ca (LMW)

These systems originate from the primordial density fluctuation spectrum of cold dark matter (e.g., Davis et al. 1985). The hierarchical clustering hypothesis leads to a picture in which subhalos are incorporated into larger systems. A number of processes such as tidal stripping and dynamical friction can lead to the destruction of substructure (White & Rees 1978). However, many subsystems survive and remain in orbit about the parent halo. This phenomenon gives birth to a large population of small satellites orbiting around galaxies and clusters of galaxies (Moore et al. 1999; Klypin et al. 1999; Ghigna et al. 2000; Diemand, Moore & Stadel 2004; Gao et al. 2004; Benson 2005). Typically this population consists of several hundred subhalos and contributes about 10% of the total dark halo mass in a galaxy (Font et al. 2001; Ghigna et al. 2000).

From an observational point of view, there is no clear evidence that such a large population of dark matter satellites exists. There are only  $\approx 40$  observed satellites in the Local Group out of which 13 belong to the Milky Way (Mateo 1998). This number is an order of magnitude less than predicted from cosmological simulations because the stellar content and hence surface brightness is below current detection limits. How then is it possible to reconcile the low number of observed satellites with models predictions? There are several possibilities that we examine below.

The satellites may still be there but difficult to observe. Many of the satellites may be associated with high-velocity clouds (Blitz et al. 1999) or may not be detected because the stellar component is not important enough and the surface brightness of these objects is below current detection limits. There are also theoretical reasons why star formation may be suppressed or inefficient in low mass satellites. Several studies explore mechanisms that should operate in the early stages of galaxy formation to suppress star formation in low-mass satellites. Gas ejection by supernovae-driven winds from the shallow potential wells of satellites may quench star formation (e.g. Dekel & Silk 1986). Also a strong intergalactic ionizing background can prevent the collapse of gas into low-mass systems (Thoul & Weinberg 1996) with circular velocities  $v_c \lesssim 30$  km/s as revealed in numerical simulations. Recently, Minchin et al. (2005) claim to have detected an HI source in the Virgo Cluster that could be a dark halo without an accompanying bright stellar galaxy. If the observed system is bound, this implies a dark halo mass up to  $10^{11} M_\odot$ . In addition, the census of the Milky Way satellites may be incomplete at low latitude due to obscuration. Willman et al. (2004) estimated a 33% incompleteness in the total number of dwarfs due to obscuration which represents only a small increase of the total number compared to cosmological predictions. All these possible explanations and considerations are plausible solutions to the satellite abundance problem.

A large satellite population may produce a strong dynamical effect and modify the

structure and kinematics of the galactic disk. Many studies look at the dynamical response of the host galaxy from an infalling satellite (Tóth & Ostriker 1992; Quinn, Hernquist & Fullagar 1993; Walker, Mihos & Hernquist 1996; Huang & Carlberg 1997; Velázquez & White 1999; Benson et al. 2004). Mihos, Walker & Hernquist (1995) show that the accretion of a low-mass satellite by a disk galaxy can generate a strong bar. This bar can buckle vertically and eject disk material out of the disk giving rise to an X-structure similar to structures observed in some bulges (e.g. Whitmore & Bell 1988). Angular momentum transfer from the satellite to the disk may also occur during the infall phase. Huang & Carlberg (1997) demonstrate that satellites with a mass  $0.3M_{\text{disk}}$  change the orientation of the disk up to  $10^\circ$  and generate warps as the satellites, under dynamical friction, sink toward the center of the galaxy. In addition, Quinn & Goodman (1986) and Quinn, Hernquist & Fullagar (1993) note that the effects on the vertical structure of the disk are not uniform across the disk. They observe some flaring of the disk at large radii, i.e. particles at large radius are orbiting at larger  $z$  than those at small radius. As suggested by these authors, a thick disk produced by minor mergers should have a scale height that increases with radius. Repeated interactions of a large population of satellites with a stellar disk also lead to disk heating. Quinn & Goodman (1986) shows that the disk is not heated isotropically by the infall of a satellite. They note that the heating is largest near the center of the disk and that most of the kinetic energy is distributed in the disk plane, i.e.  $\sigma_z$  receives a small fraction of the available energy. In fact, most of the radial and azimuthal heating comes from the disk spiral response to an infalling satellite (Quinn, Hernquist & Fullagar 1993). In addition, the disk spreads radially due to an angular momentum exchange between the satellite and the disk. Velázquez & White (1999) demonstrates that the heating and thickening rate of the disk differs for satellites on prograde and retrograde orbits. The former heat the disk and the second tilt it. Benson et al. (2004) show that there are significant differences between heating rates for prograde and retrograde orbits and those differences are amplified by increasing the mass and concentration of the satellites. As noted by some authors (Benson et al. 2004; Font et al. 2001), only satellites with orbits that bring them close to the center of the galaxy affect the disk significantly.

Most of the results described above were based on controlled numerical experiments where a single satellite interacts with a "live" disk. The exception was the pioneering study by Font et al. (2001) who examine the evolution of a stellar disk embedded in a system of several hundred subhalos. The work presented here improves upon that study in a number of ways. First, the mass resolution of our simulations is a factor of 250 higher than in the Font et al. (2001) study. This is high enough to adequately follow the evolution of the satellites and disk and to suppress two-body effects. Second, the base model for the galaxy is the self-consistent equilibrium model of M31 designed to fit the observed photometric and kinematic

data for the Galaxy. Finally, the assumed mass distribution of the subhalo population and internal structure of individual subhalos are motivated by results from cosmological simulations.

Our aim is to study the effect of tidal stripping on the satellite population. In particular, we attempt to quantify the number of satellites that survive with a detectable stellar surface brightness. (Our subhalos have a single component, but we can infer the surface brightness by modelling the stellar content, as described below.) In addition, we study the stellar halo formed from tidal debris paying particular attention to extended structures. As we will see, these structures are similar to observed features of M31 such as the Giant Stream (Ibata et al. 2001).

In §2, we describe our N-body model of M31 and describes a control experiment without satellites designed to test the model’s inherent stability. In §3, we describe the initial conditions of our satellite system. In §4, we discuss the evolution of the satellite population and follow with a discussion of the hypothesis that the metal-poor stellar halos arise in the tidal stripping of satellite galaxies. Our main conclusions are summarized in §5.

## 2. An N-body model of M31

For our experiments, we use a self-consistent numerical model of M31 derived from a composite distribution function (Widrow & Dubinski 2005) (hereafter the WD models). In general, the WD models are axisymmetric equilibrium solutions of the collisionless Boltzmann equation which may be subject to non-axisymmetric instabilities. We choose their model M31a which provides a good match to the observational data for M31. Numerical simulations of this model assuming a smooth halo find that the system is stable against the formation of a bar for 10 Gyr. Therefore any heating or instabilities that are observed in simulations where part of the smooth halo is replaced by a subhalo population should be the result of the interactions between the disk and the satellite system.

The model consists of an exponential disk, a Hernquist-model bulge and a truncated NFW halo with plausible mass-to-light ratios for the disk and bulge and simultaneous fits to the surface brightness profile, rotation curve and bulge velocity dispersion and rotation with an NFW halo that extends to the expected virial radius. These models contrast with other studies of infalling satellites (e.g Benson et al. 2004; Velázquez & White 1999) that use disk galaxy models that must be pre-relaxed from an approximate equilibrium initial state (Hernquist 1993). The M31 model has the main advantage that the initial state is formally an equilibrium solution to the collisionless Boltzmann equation since it is derived from a

distribution function constructed from integrals of motion.

Table 1 contains the physical parameters of our Andromeda model. The bulge follows the Hernquist profile

$$\rho_H(r) = \frac{\rho_b}{(r/r_b) (1 + r/r_b)^3} \quad (1)$$

while the halo is modeled according to the NFW density profile (Navarro, Frenk & White 1996)

$$\rho_{\text{NFW}} = \frac{\rho_0}{r/r_s (1 + r/r_s)^2} . \quad (2)$$

The disk distribution function is taken from Kuijken & Dubinski (1995). In brief, the surface density profile follows an exponential with scale radius  $R_d$  and truncation radius  $R_{out}$ . The vertical component is given by  $\text{sech}^2(z/z_d)$  where  $z_d$  is defined as the scale height.

## 2.1. Control Experiment Results

We first run a control experiment of the M31 system for 5 Gyr using a parallel treecode (Dubinski 1996). The softening length is 15 pc. We use 10,000 equal time steps and the total energy is conserved to within 0.7%. We take the 4.25 Gyr snapshot of the 35M-particle control model as the galaxy initial conditions for our run with satellites. Most of the initial transient spiral instabilities have died away by that time and the increase in velocity dispersion after that point is very small. Starting at this initial time minimizes the contamination of disk heating by initial transient spirals. We also run other control experiments at lower resolution (350K and 3.5M particles) to look for convergence. The simulations are run using CITA’s McKenzie cluster (Dubinski et al. 2003).

After taking the 4.25 Gyr snapshots as initial conditions, we let the galaxy evolve for 10 Gyr. Figure 1 shows the evolution of the disk velocity dispersion for the 35M model. Outside 5 kpc,  $\sigma_r$  and  $\sigma_\phi$  increase by 5-10 km s<sup>-1</sup> while  $\sigma_z$  is virtually unchanged. Inside 5 kpc, all components increase significantly. In fact, most of the heating occurs in the first few billion years where spiral patterns arising from swing-amplified noise heat the radial and azimuthal components of the velocity ellipsoid. Nevertheless, the heating is quite small and negligible in the  $z$  direction. The disk scaleheight evolution for the same model is shown in Figure 2 and found to be minimal in the inner region of the disk. There is some flaring on the edges, but the increase is only around 100 pc. The velocity dispersion ellipsoid ( $\sigma_r, \sigma_\phi, \sigma_z$ ) at an equivalent solar radius of  $R = 2.5R_d$  changes from (17.8, 24.6, 18.9) km s<sup>-1</sup> to (20.5, 29.0, 19.1) km s<sup>-1</sup> after 2.5 Gyr. In comparison, Font et al. (2001) let their disk relax for 3.5 Gyr before introducing the satellite population and their velocity dispersion ellipsoid

changes from (31, 27, 26) km s<sup>-1</sup> to (43, 30, 33) km s<sup>-1</sup>. Because we use a large number of particles for the galaxy (20M - halo, 10M - disk, 5M bulge), the mass of the halo particles are quite small and artificial disk heating due to halo particles bombarding the disk is almost negligible.

### 3. Initial conditions of the satellite population

The properties of the initial satellite population are motivated from the latest results of  $\Lambda$ CDM simulations of cluster and galaxy formation. Since the properties and distribution of subhalos do not differ significantly on galaxy and cluster size scale (Moore et al. (1999), L. Gao private communication), the different relations at cluster size scale (number density profile, slope of the mass function, total mass ratio, etc.) can be rescaled down to the galactic scale.

#### 3.1. The mass distribution function

We use the following mass function in agreement with recent  $\Lambda$ CDM simulations by (Gao et al. 2004) :

$$\frac{d\mathcal{N}}{dM} = 10^{-3.2} \left( \frac{M_{\text{sat}}}{h^{-1}M_{\odot}} \right)^{-1.9} \left( \frac{1}{h^{-1}M_{\odot}} \right)^2. \quad (3)$$

Here  $\mathcal{N}$  represents the number of satellites per unit parent mass. We distribute the satellites between  $M_{\text{sat}}/M_{\text{halo}} = 1.5 \times 10^{-4}$  to  $M_{\text{sat}}/M_{\text{halo}} = 0.02$  in 15 different logarithmic mass bins. With  $M_{\text{halo}} = 5.8 \times 10^{11} M_{\odot}$ , we get  $n \simeq 28$  and a mass fraction of 0.024. In Gao et al. (2004), Figure 12 suggests that most of the satellites for a M31-sized galaxy are in place between  $z = 0.7$  and 1.1. Their Figure 13 shows that satellites accreted at  $z = 1$  lose of order 70-80% of their mass by  $z = 0$ . With these results in mind, we start our simulation with a total mass fraction of 0.1 and 100 satellites. The sample of 100 satellites is large enough to provide the correct stochastic treatment of disk heating and will provide a smooth distribution of tidal debris. Figure 3 shows the comparison between the expected satellite cumulative mass function, the integral of Equation (3) normalized to 0.1 for  $1.5 \times 10^{-4} < M_{\text{sat}}/M_{\text{halo}} < 0.02$ , and the data points generated for our population composed of 100 satellites.

### 3.2. Spatial Distribution of Satellites

We assume that the spatial distribution of satellites in the parent halo is spherically symmetric. Recent cosmological simulations (e.g Diemand, Moore & Stadel 2004; Gao et al. 2004) suggest that the number density profile of satellites is less centrally concentrated than the dark matter halo. Gao et al. (2004) found that the cumulative number density profile of subhalos in a Milky Way size halo is well fitted by

$$N(< x) = N_{\text{tot}} x^{2.75} \frac{(1 + 0.244x_s)}{(1 + 0.244x_s x^2)} \quad (4)$$

where  $x = r/r_{200}$ ,  $x_s = r_s/r_{200}$  and  $N_{\text{tot}}$  is the total number of satellites within  $r_{200}$ . We sample that cumulative number density profile according to this formula with the further assumption that the spatial distribution of satellites is independent of the satellite mass.

### 3.3. Satellite orbital distribution

According to cosmological simulations, satellite orbits are isotropic in the center and slightly radially biased in outer regions (e.g. Benson (2005); Diemand, Moore & Stadel (2004)). The anisotropy parameter

$$\beta \equiv 1 - \frac{\sigma_\theta^2 + \sigma_\phi^2}{2\sigma_r^2} \quad (5)$$

varies with radius as  $\beta(r/r_{200}) \approx 0.35r/r_{200}$  for the satellite population (Diemand, Moore & Stadel 2004). We use a constant value of  $\beta = 0.3$  over the range  $0 < r/r_{200} < 1$  as a good approximation. The velocity components  $(\sigma_r, \sigma_\theta, \sigma_\phi)$  are determined using the Jeans equation (Binney & Tremaine 1987)

$$\frac{d(n\overline{\sigma_r^2})}{dr} + \frac{n}{r} \left[ 2\overline{\sigma_r^2} - \left( \overline{\sigma_\theta^2} + \overline{\sigma_\phi^2} \right) \right] = -n \frac{d\Phi}{dr} \quad (6)$$

where  $n$  is the satellite number density profile and  $\Phi$  is the gravitational potential. Here we assume that the gravitational potential of the host galaxy can be approximated by an NFW density profile and the gravitational potential generated by the satellite population is a small perturbation of the host gravitational potential, i.e. we neglect the contribution of the satellites. The NFW approximation is valid everywhere, except within  $\simeq 30$  kpc where the bulge and disk modify the potential significantly ( $r \lesssim 30$  kpc). We solve equation (6) numerically for  $\sigma_r(r)$  and assign the velocity  $(v_r, v_\theta, v_\phi)$  at position  $r$  assuming they are random variates with dispersions  $(\sigma_r, \beta\sigma_\theta, \beta\sigma_\phi)$ .

To validate the equilibrium of the satellite distribution within the M31 model galaxy, we replace the satellites by test particles and compute the forces assuming a rigid potential. So long as the satellites are test particles neither dynamical friction nor tidal stripping come into play. In Figure 4, we show the evolution of the cumulative number density function of satellites. There is an evolution of the distribution, but this may be attributed to small number of satellites and the inexactness of using the Jeans equations dispersion profiles to approximate the distribution function. Despite this slight evolution, we believe that our initial distribution could represent a population in quasi-equilibrium with the host galaxy and is therefore suitable for our experiments.

### 3.4. The internal structure of the satellites

Individual satellites are modeled as single cuspy NFW halos truncated by the tidal field of the galaxy model. The WD model for an isolated NFW halo has an adjustable parameter  $\gamma$  that can introduce an arbitrary tidal radius akin to the the tidal radius of a King model. Satellite models can therefore be created that have an  $r^{-1}$  cusp with NFW behavior at the extremities and a self-consistent cut-off. Many previous studies used the King model for the satellites (e.g. Benson et al. 2004; Velázquez & White 1999; Huang & Carlberg 1997) in satellite-disk interactions. Since NFW satellites are cuspy, we might expect them to be more robust to tidal interactions than King-model satellites and therefore produce more damage to the disk. We use 15 different satellite models to cover the mass range  $1.5 \times 10^{-4} < M_{\text{sat}}/M_{\text{halo}} < 0.02$  logarithmically. This mass range corresponds to  $8.75 \times 10^7 < M_{\text{sat}}/M_{\odot} < 1.17 \times 10^{10}$ . As a comparison, the Sagittarius dwarf and Large Magellanic Cloud, our galactic companions, have estimated masses of  $(2\text{-}5) \times 10^8 M_{\odot}$  (Law, Johnston & Majewski 2005; Ibata, Gilmore & Irwin 1995) and  $2 \times 10^{10} M_{\odot}$  (Schommer et al. 1992). Note that the mass of the LMC corresponds to the upper limit of the mass function. M31’s satellites M32 and NGC205 have masses of  $2.1 \times 10^9$  and  $7.4 \times 10^8 M_{\odot}$  respectively (Mateo 1998). Our mass range includes most of the observed satellites in the Local Group.

For simplicity, the truncation of each satellite is determined by the length of the tidal radius at the mean apocentric radius of the satellite system ( $r = 50$  kpc). Here we assume that the tidal radius of the satellites  $r_s$ , is defined by the Jacobi approximation (Binney & Tremaine 1987). The radial extent of the satellites is determined by comparing the mean density of the satellite inside the tidal radius and the mean density of the halo inside  $r = 50$  kpc :

$$\overline{\rho_s}(r_t) \approx 3\overline{\rho_h}(r = 50\text{kpc}) \quad (7)$$

where  $\overline{\rho_s}(r_t)$  is the satellite mean density inside the tidal radius  $r_t$  and  $\overline{\rho_h}(r = 50\text{kpc})$  is the

halo mean density inside 50 kpc. Satellites within  $r = 50$  kpc will over fill their tidal radii while those beyond will lie well within it. We determine that satellites initially located inside 50 kpc will lose a cumulative  $5.3 \times 10^8 M_{\odot}$  due to the tidal radius overestimate. This accounts for an “artificial” tidal stripping at the beginning of the simulation and corresponds to less than 1% of the total satellite mass. A true satellite system is never really in equilibrium since dynamical friction leads to continual tidal erosion so our choice of a mean satellite orbital radius for estimating the tidal radius is a compromise. We see below that there is indeed a transient startup where satellites that overfill their tidal radii are quickly stripped but by an amount that is small (less than 1%) compared the total stripping over the course of the satellite system evolution.

Table 2 contains the main characteristics of each satellite model. We model our satellites assuming a shallow power law distribution for the concentration of the satellites (Navarro, Frenk & White 1996, 1997). The internal properties of the satellite halos found in cosmological simulations are not well determined, especially for the low-mass end where the concentration and density profile are not well constrained because of the poor mass resolution.

### 3.5. Evolution of individual satellites

To compute the mass, center-of-mass position and density profile evolution of each infalling satellite, we use the technique described in Benson et al. (2004). This algorithm identifies the particles that are bound to the satellites, computes the center-of-mass of the system, and iterates until the total mass converges. Typically, the criterion we use for convergence varies by less than 0.5% in mass and most of the steps require only a few iterations. The method is straightforward and offers a good alternative to the friends-of-friends algorithm which is not appropriate when the satellites are numerous and characterized by different scale lengths.

## 4. Results

We perform two simulations at low and high resolution to test for numerical convergence. In the low resolution run, each of the one hundred satellites is represented by 1000 particles and put in orbit around an M31 galaxy model with 100K disk particles, 50K bulge particles and 200K halo particles. In the high resolution simulation, particle numbers are increased by a factor of 100. The population of satellites for both simulations have the same mass

function, spatial distribution and orbital velocities. Both simulations are run for 10 Gyr (20,000 equal time steps) using a parallelized treecode (Dubinski 1996) with opening angle parameter  $\theta = 0.9$  (quadrupole order) and  $\epsilon = 25$  pc ( $\epsilon = 15$  pc) for the 450K (45M) run. For the 45M-particle run, the energy is conserved to within 0.4 %. Unless otherwise stated, all the results presented in this section will be for the high resolution version.

## 4.1. Galaxy Evolution in Three Acts

### 4.1.1. *Act I. The First Orbit*

During the first few billion years, the satellites accomplish their first complete orbits and leave behind an interwoven web of tidal streams. Some of these streams extend beyond the virial radius of the host galaxy. One of the most interesting features of the first two billion years is the presence of shell structures with clearly defined edges similar to those seen in some elliptical galaxies. These shells are produced via phase wrapping (Quinn 1984; Hernquist & Quinn 1987) and tend to disappear quickly due to phase mixing. During this period, the disk remains quiet with only a small amount of heating.

### 4.1.2. *Act II. Bar Formation*

At about 5 Gyr, a stunning phenomenon appears in the disk : the unexpected formation of a bar. We can associate its creation with the interaction of the disk and the satellite system since no bar formed in the control run after 10 Gyr. The strong bar is responsible for most of the disk heating after 5 Gyr and creates a puffy vertical structure.

### 4.1.3. *Act III. Anticlimax : The Quiet End*

Following bar formation, the disk and satellite system evolution is more gradual. After two or three pericenter passages, the satellites are stripped significantly. The galactic halo is enriched with tidal debris and the initial streams become more mixed. The final state of the debris is that of a spheroid of about the size of the Galactic stellar halo. During that time, the bar suffers a bending instability that gives rise to the buckling mode (Raha et al. 1991). This process generates a conspicuous X-design in the disk when viewed edge-on and may point to the origin of the peanut-shaped bulges observed in many galaxies (Bureau & Freeman 1999; Kuijken & Merrifield 1995; Whitmore & Bell 1988). During the

final two billion years, the bar remains the dominant feature of the disk but slowly spins down. By the end of the simulation, a typical satellite completes five to seven orbits and loses a significant fraction of its initial mass. Snapshots of the satellite population and the host galaxy are shown in Figure 6 (see also the animation of the disk galaxy evolution at <http://www.cita.utoronto.ca/~jgauthier/m31>).

In Figures 7 and 8 we show the evolution of the disk velocity dispersion ellipsoid and scaleheight for the high-resolution run. As noted in Figure 7, the formation of the bar around 5 Gyr produces a sudden jump in velocity dispersion for disk particles. The same event triggers the scaleheight increase in Figure 8. Further details of the disk evolution will be discussed in a forthcoming paper.

#### 4.2. Evolution of the Satellite System

The satellites are initially distributed isotropically in space between approximately 50 kpc to 250 kpc ( $\approx r_{200}$ ). Although most of them survive the strong tidal interactions in the vicinity of the disk, they create extended tidal streams and shell structures. These streams and shells are particularly obvious in the first few billion years, but tend to lose their sharp edges as phase-mixing proceeds. In Figure 9, we show the evolution of the two most massive and three least massive satellites. The plots, which show the evolution of the satellites position and density profile demonstrate that dynamical friction has little effect in bringing the satellites close to the center of the galaxy. Figure 10 shows that there is no significant change to the number density profile of satellites after 10 Gyr. Because of the very steep slope of the mass function, most of our satellites have a mass of  $1.5 \times 10^{-4} M_{\text{halo}}$  and do not feel the effects of dynamical friction. In fact, plots of the satellite orbital decay indicate that the value of the apocenter radius decreases very slowly for almost all satellites, except for the very massive ones (see Figure 9).

The inner slope of the satellite density profile remains the same over the simulation (see Figure 11). As noted by Hayashi et al. (2003), it is possible to describe the structure of a stripped halo by modifying the NFW profile :

$$\rho(r) = \frac{f_t}{1 + (r/r_{\text{te}})^3} \rho_{\text{NFW}} \quad (8)$$

where  $f_t$  is interpreted as a reduction in the central density of the profile and  $r_{\text{te}}$  is an effective tidal radius that describes the cutoff due to tidal forces. Comparisons are hard to make with the work done by Hayashi et al. (2003) because our satellites suffer an initial truncation to avoid a divergent mass profile. In some way, our initial satellites density

profiles look quite similar to the final profiles of their subhalos. Nevertheless, we show, in Figure 11 the best fit of equation (8) for typical profiles of three different satellites mass bins. Equation (8) provides a good fit of the final profile especially for the low-mass satellites with  $M_{\text{sat}}/M_{\text{halo}} \lesssim 5.5 \times 10^{-4}$ . For the more massive ones, the fit tends to overestimate the mass loss at large radii.

Though only seven satellites are completely destroyed by the end of the simulation most of the remaining satellites are stripped significantly. As shown in Figure 12, the time dependence of the total mass bound in satellites can be described by two distinct phases. During the first 4 Gyr, the satellites lose approximately half their mass. The time dependence of the mass in the system is well-fit by an exponential decay :

$$M_{\text{sat}} \propto e^{-0.693t/t_{1/2}} \quad (9)$$

where  $t_{1/2} = 3.5$  Gyr. The second phase, from 4 to 10 Gyr, is quiet with  $t_{1/2} = 9.3$  Gyr. During their first complete orbit, satellites are severely stripped and lose their outer mass layers as their size becomes limited by the tidal radius at the pericentric passage. For the last 6 Gyr, the satellites radial extent is well constrained by the tidal field of Andromeda and a smaller mass loss occurs at each pericenter passage. Clearly these numbers are affected by our initial conditions and especially by the constraints on the satellites size. The position at which we compute the tidal radius of our satellites (50 kpc) is somewhat arbitrary and a different value could lead to different results. As shown in Figure 5, the distribution of the pericenter radii peaks at 50 kpc or so. Computing the tidal radius of the satellites at this position gives a good approximation of the radial extent of satellites who have completed several orbits around the galaxy (i.e. suppose to be in equilibrium with the host galaxy). Nevertheless, decreasing the radius to 30 - 40 kpc means increasing the concentration of the satellites to unrealistic values. It appears that the tidal field of the underlying halo potential is very strong and satellites falling inside 30-40 kpc must have a very high concentration to survive multiple pericenter passages. On the other hand, computing the tidal radius at say, 100 kpc and constraining the satellites to have a size less than  $r_{\text{tidal}}$  means that the satellites will reach the disk galaxy with most of their mass stripped. We think that a value of 50 kpc (4  $r_s$ ) is a reasonable choice.

### 4.3. Absence of Holmberg Effect

Holmberg (1969) showed that there is a tendency for satellite galaxies to congregate near the poles of the spiral host galaxy. His observations were then confirmed by Zaritsky et al. (1997) who showed that satellites located at large projected radii of isolated disk galaxies are

aligned preferentially along the disk minor axis. However, recent observations by Brainerd (2005) on a sample of SDSS galaxies showed that satellites are preferentially aligned with the major axis of the galaxy. This result contradicts Holmberg’s previous observations. In this paper, we examine if either of these conclusions are detected in our sample of evolved satellites and if a strong dynamical interaction between the disk and satellites at low latitudes could explain the Holmberg Effect. If dynamical friction is more important at lower latitudes, one would expect that satellites on almost coplanar orbits to sink on shorter timescales than satellites on polar orbits. That would lead to a deficit of satellites at low latitudes. In Figure 13, we show the distribution of satellites as a function of  $\cos\theta$ . The results are consistent with a uniform distribution in  $\cos\theta$ , that is a spatially isotropic distribution. In other words, we do not detect any Holmberg or anti-Holmberg effect in our simulation. We conclude that the anisotropic distribution of satellites observed around galaxies does not come from a dynamical interaction with the host galaxy but probably originates from the galaxy formation initial conditions.

#### 4.4. Outer halo stellar density profile

An important aspect of the satellite galaxy problem is their detectability. Our interest is in finding the position of the stars coming from disrupted satellites and making predictions about their distribution and luminosity. We assume that a good proxy for the initial position of stars are particles deep in the potential well of the host satellite. For our purpose, we assume that the 10% most bound particles are kinematic tracers of the stellar population in each satellite. The rationale for it is simple : as gas cools down, it loses energy and sinks in the potential well of the host satellite. Thus, we expect that most of the stars have large binding energy. Once these particles are identified, they are labeled and followed during the simulation. Each point particle represents a population of stars. To assign these particles a stellar mass, we assume a baryonic mass fraction and a star formation efficiency. We normalize the mass of these particles so that they correspond to a baryonic mass fraction of 0.171 (Steidel et al. 2003) and a star formation efficiency, the fraction of baryonic mass turned into stars, between 1 and 10% (Ricotti & Gnedin 2005). We assume a simple scenario in which the baryonic mass fraction and star formation efficiency are the same for all satellites.

We show in Figure 14 the spherically averaged density profile of “stars”. We include the stars that have been tidally disrupted from their host satellites and the ones that have not been displaced from the center of the potential well of individual satellites. The contribution from satellite stars dominate for  $r/r_{200} \geq 0.2$  and the density profile of stellar material at larger radii can be well fit by an  $r^{-3.5}$  power law that agrees with globular clusters system

(Harris 1976) of our Galaxy. This profile is also in good agreement with observations of the Milky Way's metal-poor stellar halo (Morrison et al. 2000; Chiba & Beers 2000; Yanny 2000) and with recent N-body simulations by Abadi, Navarro & Steinmetz (2005) and Bullock & Johnston (2005) who show that the density profile of the accreted stars goes as  $\rho \propto r^{-\alpha}$ ,  $\alpha \simeq 3\text{-}4$ . In addition, recent analysis of 1047 SDSS edge-on disk galaxies by Zibetti, White & Brinkmann (2004) demonstrate the presence of stellar halos with spatial distribution that is well described by a power law  $\rho \propto r^{-3}$ . Our simulation predicts that, after 10 Gyr, the satellites contribute a total stellar mass of  $1.2 \times 10^9 M_\odot$ . About 20 % of this mass is found inside the edge radius of the disk and represents less than 1 % of the total stellar mass of the disk and bulge components. The overall contribution of the satellite debris to the total galactic stellar mass is about 1%.

#### 4.5. B-band photometric maps : Streams

In order to convert surface density (which one gets from the N-body distribution) to surface brightness, one requires the mass-to-light ratio of the stellar population. This in turn requires a stellar evolution model and we use those by Bruzual & Charlot (2003)<sup>1</sup>. The resulting mass-to-light ratios in the B-band at different epochs along with the baryon fraction and the star formation history are listed in Table 3. We assume a constant  $\Upsilon = 7.6$  B-band mass-to-light ratio for M31 (Berman 2001; Faber & Gallagher 1979).

We generate  $2000 \times 2000$  pixels photometric maps showing a  $10^\circ \times 10^\circ$  field centered on M31 so that each pixel has a corresponding plate-scale of 18 arcsec. To reduce shot noise, we smooth out our “point mass stellar populations” with a 5 pixels (1.5 arcmin) gaussian window. The final results are presented in Figure 17 and represent B-band photometric maps of the stellar population expected from disrupted satellites galaxies taken at different times. We rotate our N-body model to fit the orientation of M31 on the sky. For each panel, we vary the star formation efficiency and produce three different maps.

We now examine the tidal streams in our simulations. Figure 18 presents a close-up of photometric maps at 3.5 and 5.5 Gyr. At 3.5 Gyr, there is an obvious “bridge” of stars connecting two subhalos and M31 in the upper map. This feature is similar both in morphology and brightness to the M31 giant stream detected in a number of surface density maps (Ferguson et al. 2005, 2002; Ibata et al. 2001) and constitutes the brightest stream detected in our photometric maps. The mean surface brightness of our giant stream proxy is about 28.5 mag arcsec $^{-2}$  (in the B-band) and has comparable brightness to the actual

---

<sup>1</sup>See <http://www.cida.ve/~bruzual/bc2003>

measured value of  $\mu_V \approx 30 \pm 0.5$  mag arcsec $^{-2}$  (Ibata et al. 2001). Even though we generate maps in the B-band, our photometric data in the B-band are very similar to those one would obtain in the V-band because, for a few billion year old simple stellar population, the mass-to-light ratio in the B-band is similar to the one in the V-band ( $\mu_b \approx \mu_V$  in the simulations). Other streams have also been observed around M31 and have similar brightnesses. Zucker et al. (2004) find a  $3^\circ$  overdensity of luminous red giant stars (Andromeda NE) having a central g-band surface brightness of 29 mag arcsec $^{-2}$ . In addition, McConnachie et al. (2004) observe an arc-like overdensity of blue, red giant stars in the west quadrant of M31. This tail has a  $\mu_V = 28.5 \pm 0.5$  mag arcsec $^{-2}$ . Similarly, the G1 Clump, a stellar overdensity that is located 30 kpc along the southwestern major axis could be associated by an overdense clump locate at the lower right edge of Andromeda in bottom picture of Figure 18.

#### 4.6. Surface Brightness Profile

In Figure 16 we show the surface brightness profiles of the stars no longer bound to the satellites and contributing to the metal-poor halo of M31. The plots are drawn assuming a star formation efficiency of 10% and a simple stellar population formed 1 Gyr prior to the beginning of the simulation. Comparisons with actual observations of the surface brightness profile of M31 are quite challenging because the extremely low surface brightnesses involved pose a significant problem for observers (typically, 7-8 mag higher than the sky). One of the deepest surveys of M31 halo surface brightness was carried out by Irwin et al. (2005). These authors have been able to go down to  $\mu_V \approx 32$  mag arcsec $^{-2}$  at a projected radius (along the minor axis) of  $4^\circ$  (55 kpc). At that radius, they obtain a V-band surface brightness of about 30-31 mag arcsec $^{-2}$  which is close to our B-band estimate of 29-30 mag arcsec $^{-2}$ . In Figure 16, a star formation efficiency of 5% would decrease the surface brightness at all radii by about  $+0.75$  mag arcsec $^{-2}$  and leads to a better agreement with the value measured at 55 kpc.

The value of the surface brightness for  $R < 50$  kpc flattens at about 28 mag arcsec $^{-2}$ . Dynamical friction only weakly affects the trajectories of the satellites and thus, little mass is being deposited in the center of the galaxy. Other studies (e.g. Abadi, Navarro & Steinmetz (2005)) show a constant increase of the surface brightness profile down to a radius of about 10 kpc. In many simulations, the satellites sink in the center of the galaxy and get heavily stripped within 30 kpc and deposit large amounts of mass in the center. It is not the case in this simulation.

#### 4.7. Satellites detected around M31

A way of constraining the star formation history of the satellites is by counting the number of satellites detected in the close vicinity of M31 as a function of the star formation efficiency and epoch of birth and compare their number and properties with the current 16 M31 satellites claimed by McConnachie & Irwin (2005). The faintest of these satellites is Andromeda IX ( $\mu_V = 26.8$  mag arcsec $^{-2}$ ) discovered by Zucker et al. (2004). The survey is complete for satellites with  $\mu_V < 26.8$  mag arcsec $^{-2}$ . According to the results listed in Table 4, it appears that a star formation rate of about 10% combined with an epoch of formation between 3.5 and 1 Gyr prior to the beginning of the simulation can account for the actual number of satellites detected around M31. For the 5.5 Gyr snapshots, a star formation rate of 10% results in exactly 15 detected satellites with  $\mu_V < 26.8$  mag arcsec $^{-2}$ . On the other hand, a SFR of 1% is insufficient since it reduces to 0 the number of satellites detected below the 26.9 mag arcsec $^{-2}$  limit.

We expect the most massive satellites to have a light distribution similar to M32 or NGC 205. The galaxies have, respectively, a central B-band surface brightness of approximately 17.5 mag arcsec $^{-2}$  and 20 mag arcsec $^{-2}$  (Choi, Guhathakurta & Johnston 2002) . The brightest simulated satellites located in the vicinity of M31 have a central B-band surface brightness of about 23 mag arcsec $^{-2}$  assuming a simple stellar population formed 1.5 Gyr before the beginning of the simulation and and a star formation efficiency of 10%. The fact that our simulations are dissipationless is the cause of this difference. In a more realistic case, gas cools down and sink deep in the potential well increasing the central density of stars. Our simulations provide lower limits to the value of the central surface brightness one would expect. However, a central value of 22-23 mag arcsec $^{-2}$  is consistent with a recent study of dwarf galaxies in the Fornax cluster (Phillipps et al. 2001). These authors find that the majority of the dwarfs in their sample have a surface brightness spanning 20 - 24 mag arcsec $^{-2}$  (see their Figure 1). Many of our satellites would fall in that range of central brightness.

The surface brightness at the half-light is a more representative measurement of the overall dwarf light distribution and does not suffer much from dissipation effects. Our brightest satellites have  $\mu_{eff,b} = 25.3$  mag arcsec $^{-2}$ . By comparison, M32 has a half-light surface brightness  $\mu_{eff,B} \approx 20$  mag arcsec $^{-2}$  (Choi, Guhathakurta & Johnston 2002). A more recent episode of star formation or a continuous star forming period could explain that difference since younger stars would increase the B-band flux emission. Our simple model assume that all stars have the same age and in this case, formed 1.5 Gyr before the beginning of the simulation. We conclude that our brightest satellites show photometric differences with the most massive companions of M31. However, our simulations are purely collisionless and

including dissipative processes would increase the central and half-light radius luminosities in such a way that the brightest simulated satellites would be similar to M32 and NGC205.

Our choice of a satellite mass range of  $1.5 \times 10^{-4} < M_{\text{sat}}/M_{\text{halo}} < 0.02$  is consistent with approximately 100 satellites according to measured numbers in cosmological simulations. However, if we extend the mass range to lower and higher values there would be many more dark matter satellites, especially at the lower mass end. These satellites might potentially be detectable, add more stars to the tidal debris stellar halo, and thus change our conclusions. We therefore estimate the effects of the satellite mass range on the final total number of satellites that might be detected near M31. We sample the same mass function as equation (3) but this time with lower and upper limits  $1.5 \times 10^{-5} < M_{\text{sat}}/M_{\text{halo}} < 0.1$  that leads to about 1,000 satellites with a total combined mass of  $0.25 M_{\text{halo}}$  compared with a total satellite mass of  $0.1 M_{\text{halo}}$  for our 100 satellite run. By extending the mass range, we add nearly 900 low mass halos and five high mass ones outside the original range. The six most massive halos would account for  $0.16 M_{\text{halo}}$  and would be easily detected having a central surface brightness greater than 27 mag arcsec $^{-2}$  even with significant stripping as seen in our simulation. However, the 900 additional low mass halos would probably be fainter than 32 mag arcsec $^{-2}$ , the central surface brightness of the lowest mass satellites in our run. More than 60% of them have a mass less than  $2.5 \times 10^{-5}$  and have central brightnesses of 34 mag arcsec $^{-2}$  according to a linear extrapolation of our results. None of this population would be detected in the current surveys of the M31 stellar halo region so our exclusion of the low mass tail of satellite population has little effect on the predictions for the number of satellites around M31. However, the low mass satellites contain a significant amount of mass and tidal stripping of this population could approximately double the amount of tidal debris in the stellar halo. Surface brightness maps might then be expected to be a magnitude higher than what our 45M particle simulation predicts.

## 5. Summary & Conclusion

This study presents the evolution of a self-consistent population of satellites in the presence of a parent galaxy. The internal structure, mass function and spatial and orbital distribution of the satellite distribution is motivated by cosmological simulations. The work improves upon previous self-consistent studies (e.g. Font et al. 2001) by using a more realistic galaxy model and much improved numerical resolution. It follows the lead of current work on satellite tidal disruption to make quantitative predictions of the tidal debris field of galaxies (e.g. Johnston, Sackett & Bullock 2001).

This work shows that members of a typical population of subhalos orbiting in a galactic

will come close to the disk with a ten billion years timescale. In addition, it is possible to model these satellites and make direct predictions on the number one would expect to detect around a typical galaxy. We also agree that it is possible to maintain a disk in spite of substructure having a mass fraction of about  $0.1M_{\text{halo}}$ .

Here we summarize the main results of this paper.

1. Dynamical friction plays only a minor role in the evolution of the satellite system and the number density profile of the system is relatively unchanged over 10 Gyr. The orbits of the most massive satellites do show some decay but since they suffer severe tidal stripping, dynamical friction quickly becomes unimportant.
2. The vast majority of the satellites survive in the galactic environment for more than a Hubble time; only 7 are completely disrupted. However, most of satellites lose a significant fraction of their mass due to tidal interactions.
3. The satellite mass loss due to tidal stripping is described by two distinct phases. The first one is characterized by a sharp mass decline with  $t_{1/2} = 3.5$  Gyr. During that period, a small amount of mass loss,  $5.3 \times 10^8 M_{\odot}$ , is due to a transient state where satellites initially located inside 50 kpc are overfilling their tidal radius and start losing mass instantly. During the second phase, the satellites lose about 25% of their initial mass with  $t_{1/2} = 9.3$  Gyr. Over 10 Gyr, the satellite population mass diminishes by about 75% and turns into tidal debris. These debris form long tidal tails around the galaxy and can be detected in photometric maps of M31. The final density profile of the light satellites can be approximated by the fitting function given in Hayashi et al. (2003).
4. The spatial distribution of stars associated with infalling satellites follow a power law  $\rho \propto r^{-3.5}$  at large radii. This result is in agreement with recent numerical studies and observations of the stellar halo in edge-on disk galaxies.
5. No obvious Holmberg Effect is observed.
6. The mock B-band photometric maps, computed under the assumption that the most tightly bound particles are kinematic tracers of the stars, show conspicuous features of bridges and tails comparable to what is actually observed. A star formation efficiency of 10% is necessary to match the morphological and photometric properties of our Giant Stream proxy with the real one.
7. The number of satellites detected around M31 below  $\mu_V \approx 26.8$  mag arcsec $^{-2}$  can match our results with a star formation efficiency of 10%. For a value of 1%, the

number of satellites detected goes down to 0. A value of 5% can not be discarded since dissipation is not taken into account. Many of the satellites between 26.8 and 29.4 mag arcsec $^{-2}$  in a 5% star formation efficiency scenario would probably be detected under the limit of 26.8 mag arcsec $^{-2}$  if dissipation was included in the simulations.

8. A star formation efficiency of about 5% is necessary to account for the actual M31 value of the surface brightness of the stellar halo measured at 55 kpc. Comparisons for radii larger than 55 kpc are observationally challenging because of the very low surface brightness in the outer parts of the galaxy. The simulated maps show a flattening in the inner part of the surface brightness profile (for  $R < 55$  kpc,  $\mu_B \approx 28$  mag arcsec $^{-2}$ ) showing that dynamical friction is unable to bring the satellites close to the center. Most of the mass is lost at larger radii.
9. The formation of a bar around 5 Gyr is the result of interactions of satellites with the disk. This intriguing result will be discussed in a forthcoming paper.

JRG would like to acknowledge support from NSERC postgraduate scholarship. JD and LMW acknowledge research support from NSERC. We would like to thank Amr A. El-Zant for helpful discussions and comments. All simulations were run on the McKenzie Beowulf Cluster at the Canadian Institute for Theoretical Astrophysics funded by the Canadian Foundation for Innovation and the Ontario Innovation Trust.

## REFERENCES

Abadi, M.G., Navarro, J.F., Steinmetz, M. 2006, MNRAS, 365, 747

Benson, A.J. 2005, MNRAS, 358, 551.

Benson, A.J., Lacey, C.G., Frenk, C., Baugh, C.M., Cole, S., 2004, MNRAS, 351, 1215

Berman, J. 2001,  $\text{\aa}$ , 371, 476B

Binney, J., Tremaine, S., Galactic Dynamics (Princeton Univ. Press)

Blitz, L., Spergel, D., Teuben, P., Hartmann, D., Burton, W.B. 1999, ApJ, 574, 818

Brainerd, T.G. 2005, ApJ, 628, L101

Bruzual, G., Charlot, S. 2003, MNRAS, 344, 1000

Bullock, J.S., Johnston, K.V. 2005, ApJ, 635, 931

Bureau, M., Freeman, K.C. 1999, ApJ, 118, 126

Chiba, M., Beers, T.C. 2000, AJ, 119, 2843

Choi, P.I., Guhathakurta, P., Johnston, K.V. 2002, ApJ, 124, 310

Davis, M., Efstathiou, G., Frenk, C.S., White, S.D.M. 1985, ApJ, 292, 371

Dekel, A., Silk, J. 1986, ApJ, 303, 39

Diemand, J., Moore, B., Stadel, J. 2004, MNRAS, 352, 535

Dubinski, J. 1996, *NewA*, 1, 133

Dubinski, J., Humble, R.J., Loken, C., Pen, U.-L. Martin, P.G. 2003, “McKenzie: A Teraflops Linux Beowulf Cluster for Computational Astrophysics”, Proc. of the 17th Annual International Symposium on High Performance Computing Systems and Applications, May 11-14, 2003, Sherbrooke, PQ

Faber, S.M., Gallagher, J.S. 1979 ARA&A, 17, 135

Ferguson, A.M., Irwin, M.J., Ibata, R.A., Lewis, G.F., Tanvir, N.R. 2002, AJ, 124, 1452

Ferguson, A.M., Johnson, R.A., Faria, D.C., Irwin, M.J., Ibata, R.A., Johnston, K.V., Lewis, G.F., Tanvir, N.R. 2005, ApJ, 622, L109

Font, A.S., Navarro, J.F., Stadel, J., Quinn, T., 2001, ApJ, 563, L1

Gao, L., White, S.D.M., Jenkins, A., Stoehr, F., Springel, V. 2004, MNRAS, 355, 819

Ghigha, S., Moore, B., Governato, F., Lake, G., Quinn, T., Stadel, J., 2000, ApJ, 544, 616

Harris, W.E. 1976, AJ, 81, 1095

Hayashi, E., Navarro, J.F., Taylor, J.E., Stadel, J., Quinn, T. 2003, ApJ, 584, 541

Hernquist, L., Quinn, P.J. 1987, ApJ, 312, 1

Hernquist, L. 1993, ApJS, 86, 389

Holmberg, E. 1969, Ark. Astron., 5, 305

Huang, S., Carlberg, R.G., 1997, ApJ, 480, 503

Ibata, R.A., Gilmore, G., Irwin, M.J. 1995, MNRAS, 277, 781

Ibata, R.A., Irwin, M., Lewis, G., Ferguson, A.M.N., Tanvir, N. 2001, Nature, 412, 49,

Irwin, M.J., Ferguson, A.M.N., Ibata, R.A., Lewis, G.F., Tanvir, N.R. 2005, ApJ, 628, L105

Johnston, K.V., Sackett, P.D., Bullock, J.S. 2001, ApJ, 557, 137

Kuijken, K., Dubinski, J. 1995 MNRAS, 277, 1341

Kuijken, K., Merrifield, M.R. 1995, ApJ, 443, L13

Klypin, A., Kravtsov, A.V., Valenzuela, O., 1999, ApJ, 522, 82

Law, D.R., Johnston, K.V., Majewski, S.R. 2005, ApJ, 619, 807

Mateo, M.L., 1998 *ARA&A*, 36, 435

McConnachie, A.W., Irwin, M.J. 2006, MNRAS, 365, 1263

McConnachie, A.W., Irwin, M.J., Lewis, G.F., Ibata, R.A., Chapman, S.C., Ferguson, A.M.N., Tanvir, N.R. 2004, MNRAS, 351, L94

Mihos, J.C., Walker, I.R., Hernquist, L. 1995, ApJ, 447, L87

Minchin, R., Davies, J., Disney, M., Boyce, P., Garcia, D., Jordan, C., Kilborn, V., Lang, R., Roberts, S., Sabatini, S., van Driel, W. 2005 astro-ph/0502312

Morrison, H.L., Mateo, M., Olszewski, E.W., Harding, P., Dohm-Palmer, R.C., Freeman, K.C., Norris, J.E., Morita, M. 2000, AJ, 119, 2254

Moore, B., Ghigna, S., Governato, F., 1999, ApJ, 524, L19

Navarro, J.F., Frenk, C.S., White, S.D.M. 1996, ApJ, 462, 563

Navarro, J.F., Frenk, C.S., White, S.D.M. 1997, ApJ, 490, 493

Phillipps, S., Drinkwater, M.J., Gregg, M.D., Jones, J.B. 2002, ApJ, 560, 201

Quinn, P.J. 1984, ApJ, 279, 596

Quinn, P.J., Goodman, J. 1986, ApJ, 309, 472

Quinn, P.J., Hernquist, L., Fullagar, D.P. 1993, ApJ, 403, 74

Raha, N., Sellwood, J.A., James, R.A., Kahn, F.D. 1991, Nature, 352, 411

Ricotti, M., Gnedin, N.Y. 2005, ApJ, 629, 259

Schommer, R.A., Olszewski, E.W., Suntzeff, N.B., Harris, H.C. 1992, ApJ, 103, 447

Steidel, C.C. et al. 2003, ApJS, 148, 175

Thoul, A.A., Weinberg, D.H. 1996, ApJ, 465, 608

Tóth G., Ostriker, J.P., 1992, ApJ, 389, 5

Velázquez, H., White, S.D.M., 1999, MNRAS, 304, 254

Walker, I.R., Mihos, J.C., Hernquist, L. 1996, ApJ, 460, 121

White, S.D.M., Rees, M.J., 1978, MNRAS, 183, 341

Whitmore, B.C., Bell, M. 1988, ApJ, 324, 741

Widrow, L.M., Dubinski, J., 2005, ApJ, 631, 838

Willman, B., Governato, F., Dalcanton, J.J., Reed, D., Quinn, T. 2004, MNRAS, 353, 639

Yanny, B. 2000, ApJ, 540, 825

Zaritsky, D., Smith, R., Frenk, C., White, S.D.M. 1997, ApJ, 478, L53

Zibetti, S., White, S.D.M., Brinkmann, J. 2004, MNRAS, 347, 556

Zucker, D.B. et al. 2004, ApJ, 612, L117

Zucker, D.B. et al. 2004, ApJ, 612, L121

Table 1. Andromeda (M31) model

Component	Parameter	Value
Disk	Mass	$7.77 \times 10^{10} M_{\odot}$
	$R_D$	5.57 kpc
	$z_D$	1.0 kpc
	$R_{out}$	30 kpc
Bulge	Mass	$2,88 \times 10^{10} M_{\odot}$
	$r_b$	1.82 kpc
	$v_b^a$	460 km/s
	cut-off	0.929
Halo	Mass	$5.83 \times 10^{11} M_{\odot}$
	$r_s$	12.93 kpc
	$v_s$	337 km/s
	$c$	13.37
	edge radius	232.3 kpc
	cut-off	0.75

Table 2. Physical parameters of the satellite models.

Name	$M_{\text{sat}}/M_{\text{halo}}$	$r_s$ [kpc]	$v_s$ [km/s]	cutoff	$M(< r_{\text{tid}}/M_{\text{sat}})$	c
NFW1	$1.5 \times 10^{-4}$	0.7	50	0.4	0.97	29.4
NFW2	$2.5 \times 10^{-4}$	0.85	56	0.4	0.96	27.7
NFW3	$3.5 \times 10^{-4}$	0.98	62	0.4	0.92	26.8
NFW4	$4.5 \times 10^{-4}$	1.1	65	0.4	0.91	25.4
NFW5	$5.5 \times 10^{-4}$	1.2	70	0.4	0.95	25.2
NFW6	$6.5 \times 10^{-4}$	1.33	75	0.4	0.94	24.5
NFW7	$7.5 \times 10^{-4}$	1.39	77	0.4	0.94	24.2
NFW8	$8.5 \times 10^{-4}$	1.46	80	0.4	0.95	24.0
NFW9	$9.5 \times 10^{-4}$	1.54	82	0.4	0.94	23.5
NFW10	$1.5 \times 10^{-3}$	1.79	93	0.4	0.93	23.0
NFW11	$2.5 \times 10^{-3}$	2.2	112	0.4	0.91	22.7
NFW12	$3.5 \times 10^{-3}$	2.5	122	0.4	0.89	21.9
NFW13	$5.5 \times 10^{-3}$	3.09	141	0.4	0.88	20.8
NFW14	$6.5 \times 10^{-3}$	3.35	146	0.4	0.87	20.1
NFW15	$2 \times 10^{-2}$	5.5	200	0.4	0.77	17.5

Table 3. B-band photometric maps parameters

Kinematic tracers :	10 % most bound particles
Baryonic mass fraction ( $M_b/M_{\text{DM}}$ ) :	0.171 <sup>a</sup>
Star formation efficiency <sup>b</sup> ( $M_{\star}/M_b$ ) :	0.01, 0.05 and 0.1
M31 $M/L_B$ (constant) <sup>c</sup> : 7.6	
For a simple stellar population formed at $t = -1^e$ Gyr :	
$M/L_B$ ratio at $t=3.5$ Gyr :	1.5476 <sup>d</sup>
$M/L_B$ ratio at $t=5.5$ Gyr :	2.0771
$M/L_B$ ratio at $t=9.5$ Gyr :	2.9688
For a simple stellar population formed at $t = -2.5$ Gyr :	
$M/L_B$ ratio at $t=3.5$ Gyr :	1.9485
$M/L_B$ ratio at $t=5.5$ Gyr :	2.4115
$M/L_B$ ratio at $t=9.5$ Gyr :	3.2855
For a simple stellar population formed at $t = -3.5$ Gyr :	
$M/L_B$ ratio at $t=3.5$ Gyr :	2.1877
$M/L_B$ ratio at $t=5.5$ Gyr :	2.6631
$M/L_B$ ratio at $t=9.5$ Gyr :	3.4411

<sup>a</sup>Steidel et al. (2003)

<sup>b</sup>Ricotti & Gnedin (2005)

<sup>c</sup>Faber & Gallagher (1979)

<sup>d</sup>GALAXEV code, Bruzual & Charlot (2003)

<sup>e</sup>Note that the simulation starts at  $t=0$ . We imply here that the stars formed prior to the beginning of the simulation.

Table 4. Number of satellite galaxies detected in a  $10^\circ \times 10^\circ$  field centered on M31 for different stellar population ages, star formation efficiency and isophotal thresholds

$t_{\text{form}}$ (Gyr)	$t_{\text{meas}}^a$ (Gyr)	$M_\star/M_{\text{bar}}$	$N \leq 26.89 \text{ mag arcsec}^{-2}$	$N \leq 29.4 \text{ mag arcsec}^{-2}$	$N \leq 31.9 \text{ mag arcsec}^{-2}$
-1	3.5	0.01	1	23	26
-1	3.5	0.05	11	26	26
-1	3.5	0.1	25	26	26
-1	5.5	0.01	0	15	30
-1	5.5	0.05	6	30	30
-1	5.5	0.1	15	30	30
-1	9.5	0.01	0	8	29
-1	9.5	0.05	4	30	30
-1	9.5	0.1	8	30	30
-2.5	3.5	0.01	0	23	26
-2.5	3.5	0.05	10	26	26
-2.5	3.5	0.1	23	26	26
-2.5	5.5	0.01	0	13	30
-2.5	5.5	0.05	6	30	30
-2.5	5.5	0.1	15	30	30
-2.5	9.5	0.01	0	8	29
-2.5	9.5	0.05	3	30	30
-2.5	9.5	0.1	7	30	30
-3.5	3.5	0.01	1	20	26
-3.5	3.5	0.05	9	26	26
-3.5	3.5	0.1	22	26	26
-3.5	5.5	0.01	0	12	30
-3.5	5.5	0.05	6	30	30
-3.5	5.5	0.1	15	30	30
-3.5	9.5	0.01	0	7	29
-3.5	9.5	0.05	3	30	30
-3.5	9.5	0.1	7	30	30

<sup>a</sup>The time at which the measurements are made after the beginning of the simulation.

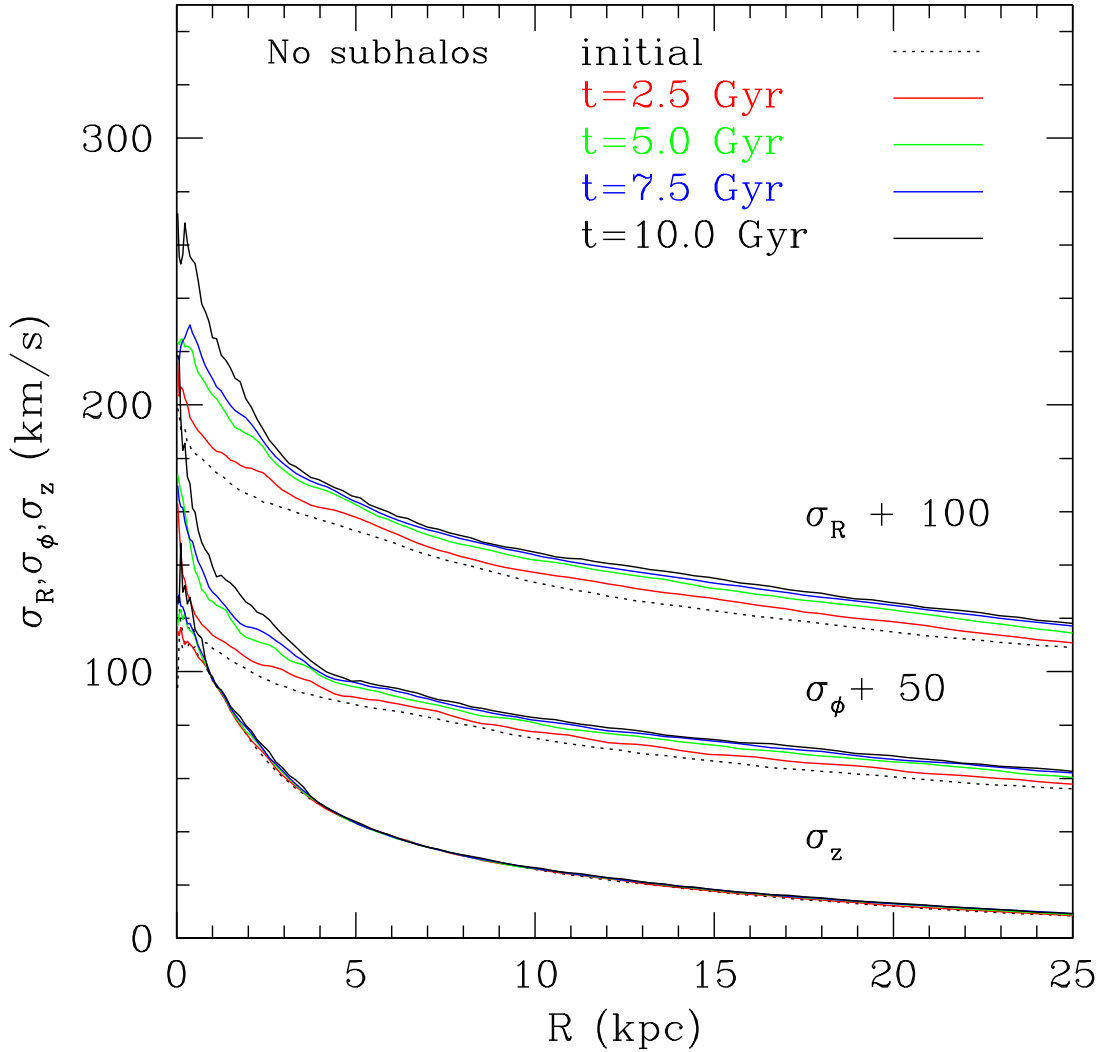


Fig. 1.— Evolution of the disk velocity dispersion for the 35M control simulation. From bottom to top :  $\sigma_z$ ,  $\sigma_\phi + 50$  km/s and  $\sigma_r + 100$  km/s. Note that there is no vertical heating over 10 Gyr. Most of the heating in the radial and azimuthal directions occurs in the first 5 Gyr and is due to transient spiral features present early in the simulation.

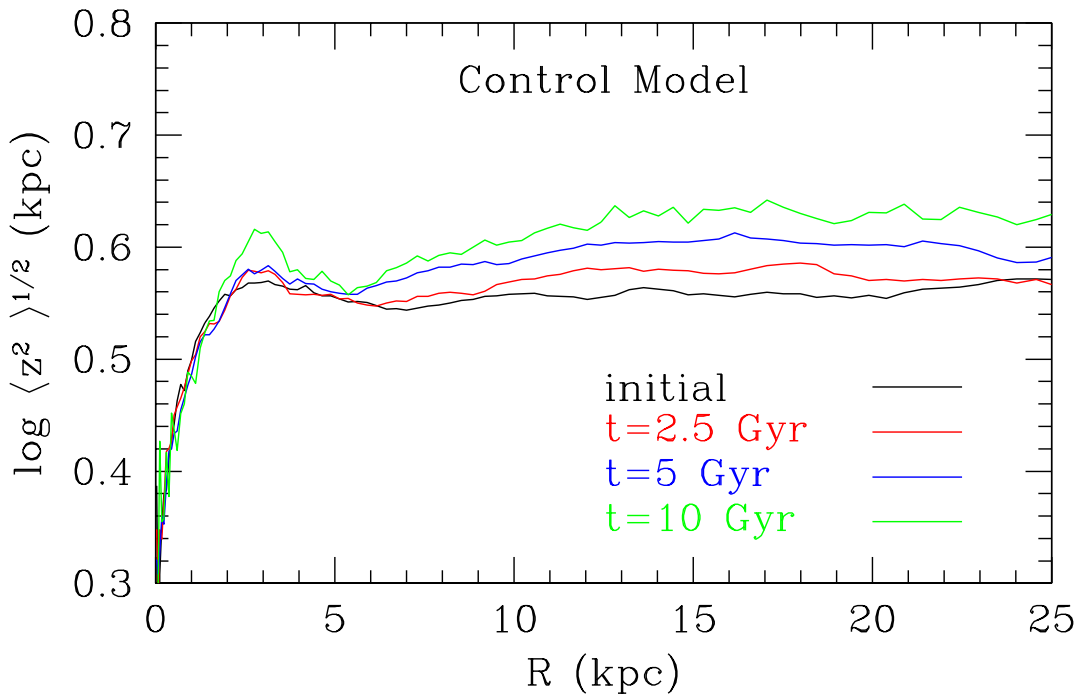


Fig. 2.— Disk scale height versus radius for the control experiment. Scale height is taken to be the variance of  $z$  averaged over circular rings in the disk. Note that there is only minor growth of the scale height with time reflecting the quiet equilibrium of the disk DF and adequate resolution of the simulation.

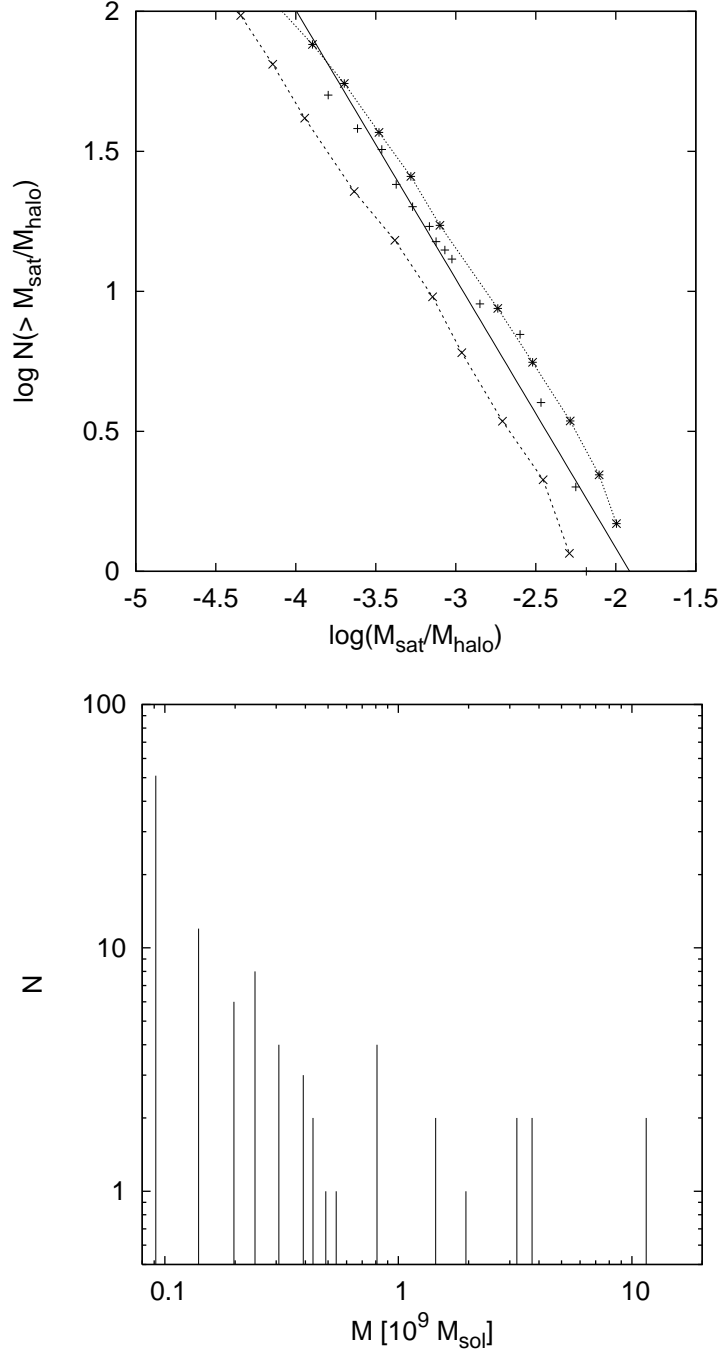


Fig. 3.— Satellite cumulative mass function (top) and mass function (bottom). For the top figure, the *plus* symbols are the data points for our mass function and the *filled* line is the best  $dn/dM_{\text{sat}} \propto M_{\text{sat}}^{-1.9}$  fit to the data. Note that the mass function we use is normalized in such a way that in the interval  $1.5 \times 10^{-4} < M_{\text{sat}}/M_{\text{halo}} < 0.02$  the total mass in subhalos is  $0.1 M_{\text{halo}}$ . The other lines with symbols are taken from Gao et al. (2004). The *X* symbols and *short-dashed* line represent the subhalo mass function of a high resolution  $2 \times 10^{12} M_{\odot}$  halo (GA3n run). The *star* symbols and the *dotted* line refer to an average of all the cluster-type simulations.

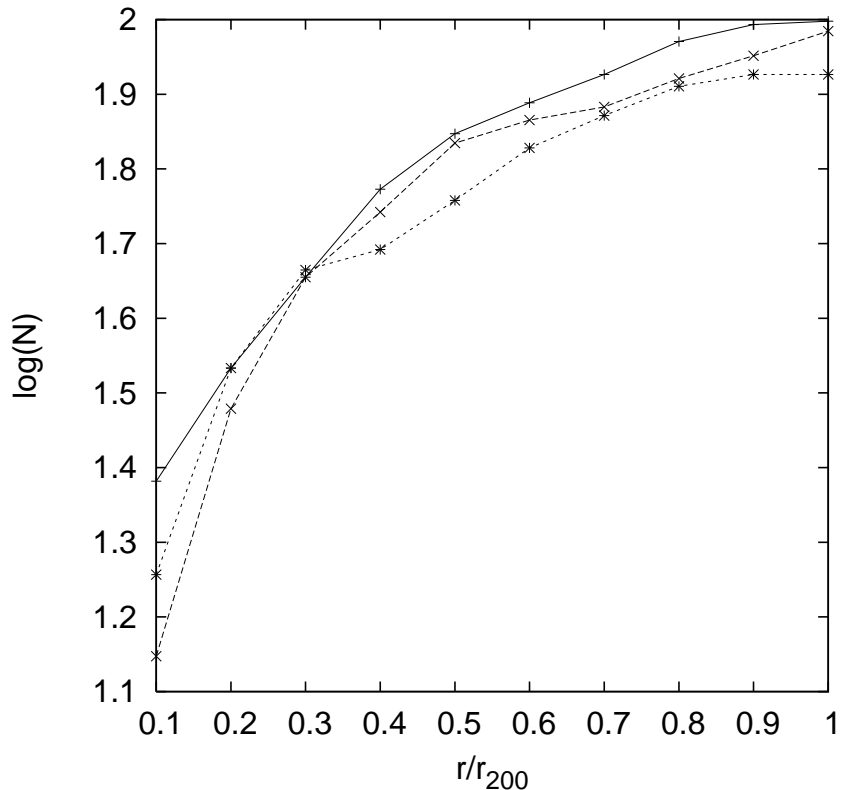


Fig. 4.— Evolution of the satellite cumulative number density function using solid test particles in the rigid M31 potential (no dynamical friction/tidal stripping). The different lines with symbols are for : *plus-filled* 0 Gyr, *X-dashed* 5 Gyr, and *stars-dotted* 10 Gyr snapshot. The cumulative number density function evolves slightly over 10 Gyr reflecting the small number statistics and the fact that spherical NFW potential is only an approximation to the full potential for the galactic model.

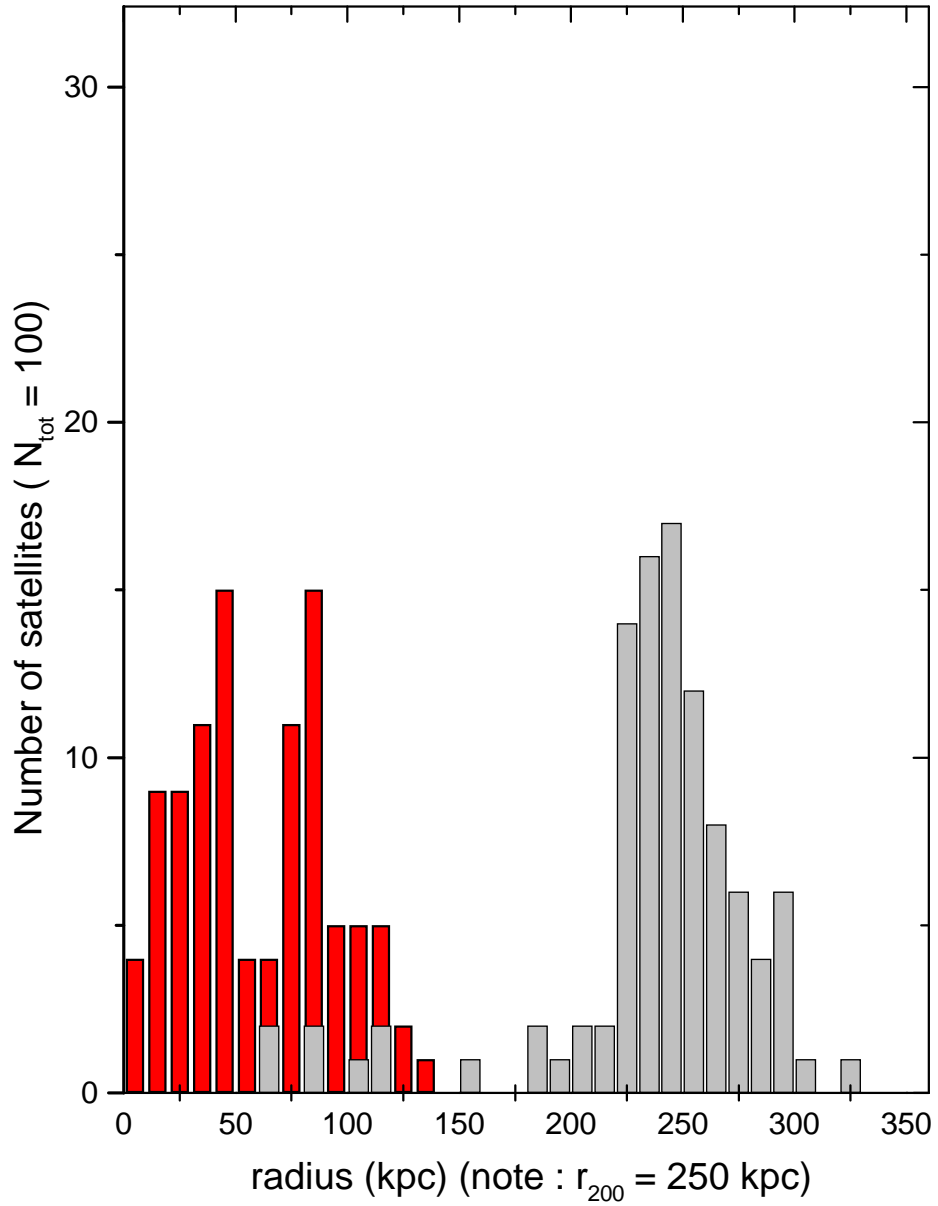


Fig. 5.— Distribution of the initial pericenter and apocenter passages radii for the satellites population. In *red* : the pericenter radii; in *gray* : apocenter radii. The pericenter distribution peaks at 50 kpc and the apocenter one at 250 kpc. The ratio  $r_a/r_p \approx 5$  is typical of cosmological simulations (e.g. Moore et al. (1999)).

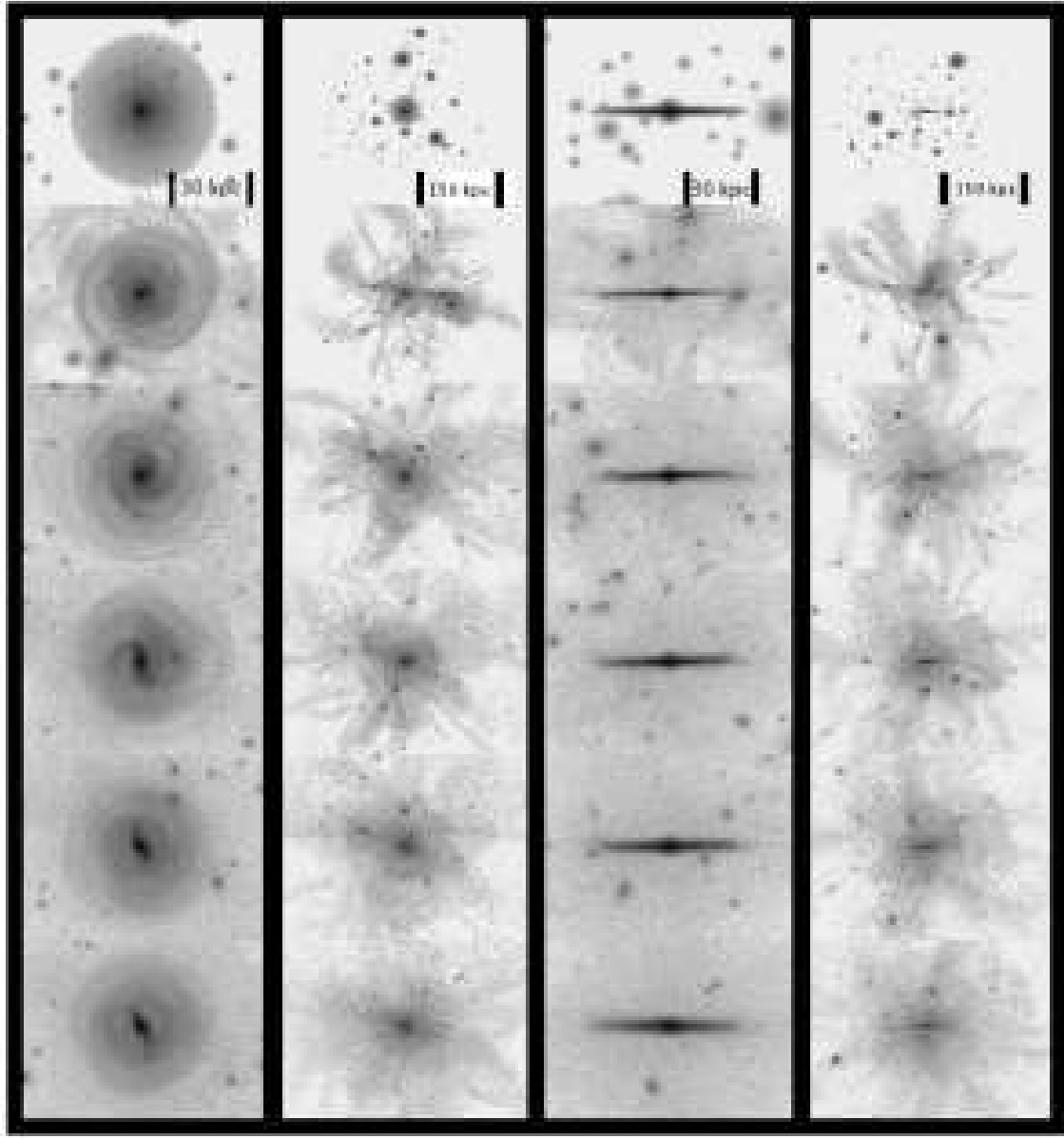


Fig. 6.— Snapshots of the 100-satellite simulation. From top to bottom,  $t=0, 2, 4, 6, 8$ , and  $10$  Gyr. One can see that a strong bar is formed between 4 and 6 Gyr. Several conspicuous shell structures are visible, especially in the first few billion years. (See high-resolution color snapshots at <http://www.cita.utoronto.ca/~jgauthier/m31>)

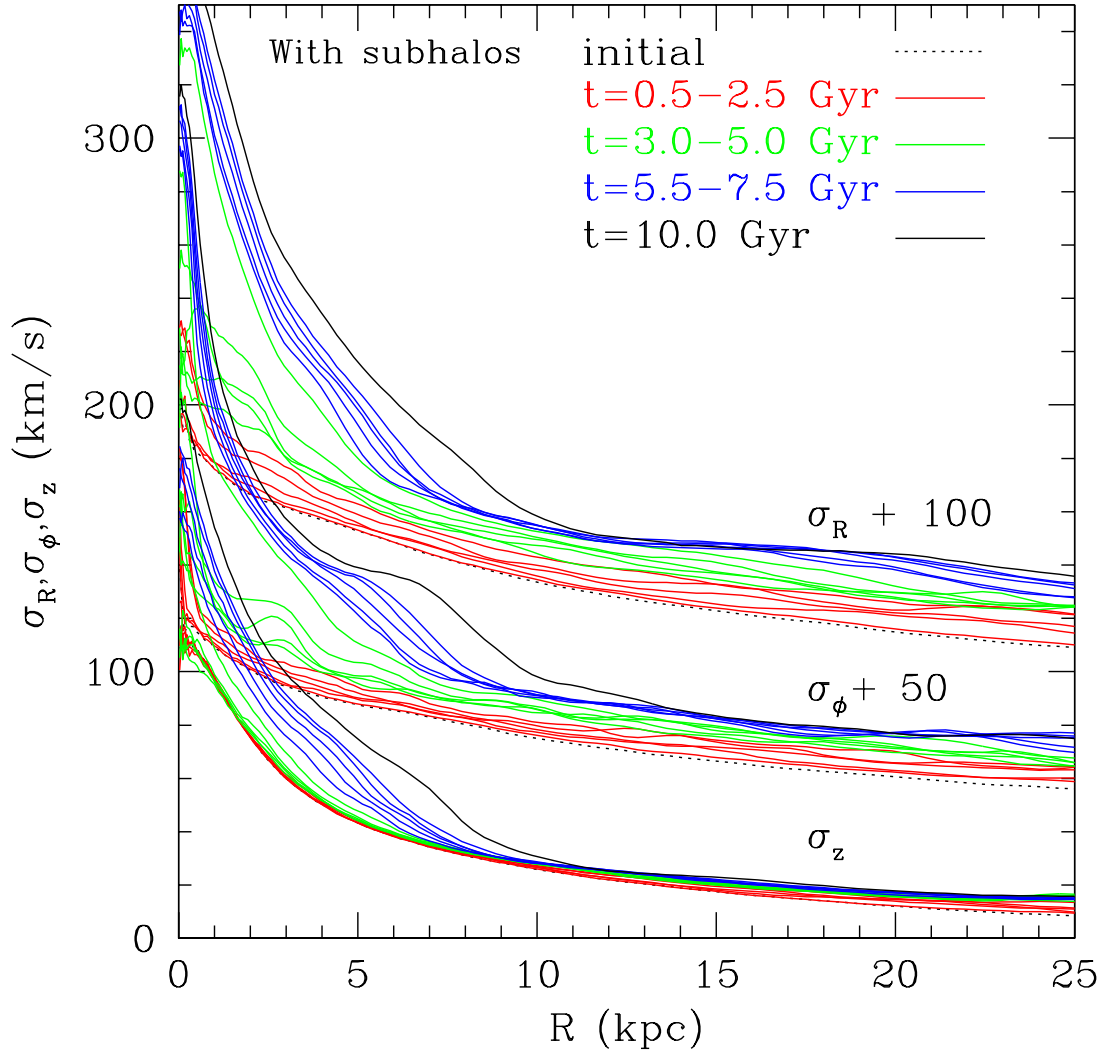


Fig. 7.— Evolution of the disk velocity dispersion for the simulation with subhalos. From bottom to top :  $\sigma_z$ ,  $\sigma_\phi + 50$  km/s and  $\sigma_r + 100$  km/s. Between 4 and 5 Gyr, a bar forms. This explains the sudden increase of  $\sigma_r$  and  $\sigma_\phi$  in the inner region of the galaxy between 3 and 5 Gyr.

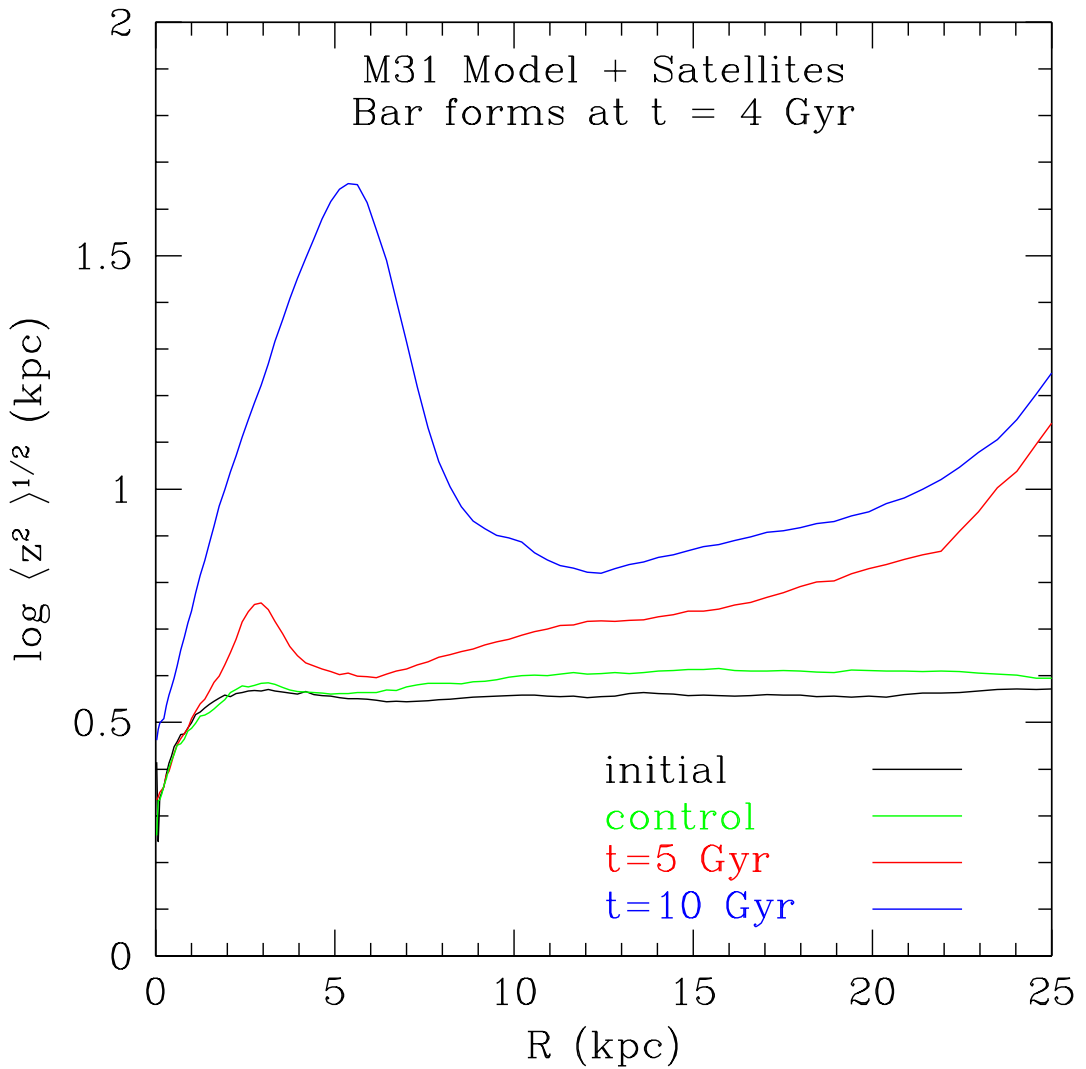


Fig. 8.— Same as Figure 2 but with satellite population. The scale height only grows slightly during the first 4 billion years reflecting only mild heating from the satellite population. The rapid heating thereafter is due to the formation of the bar.

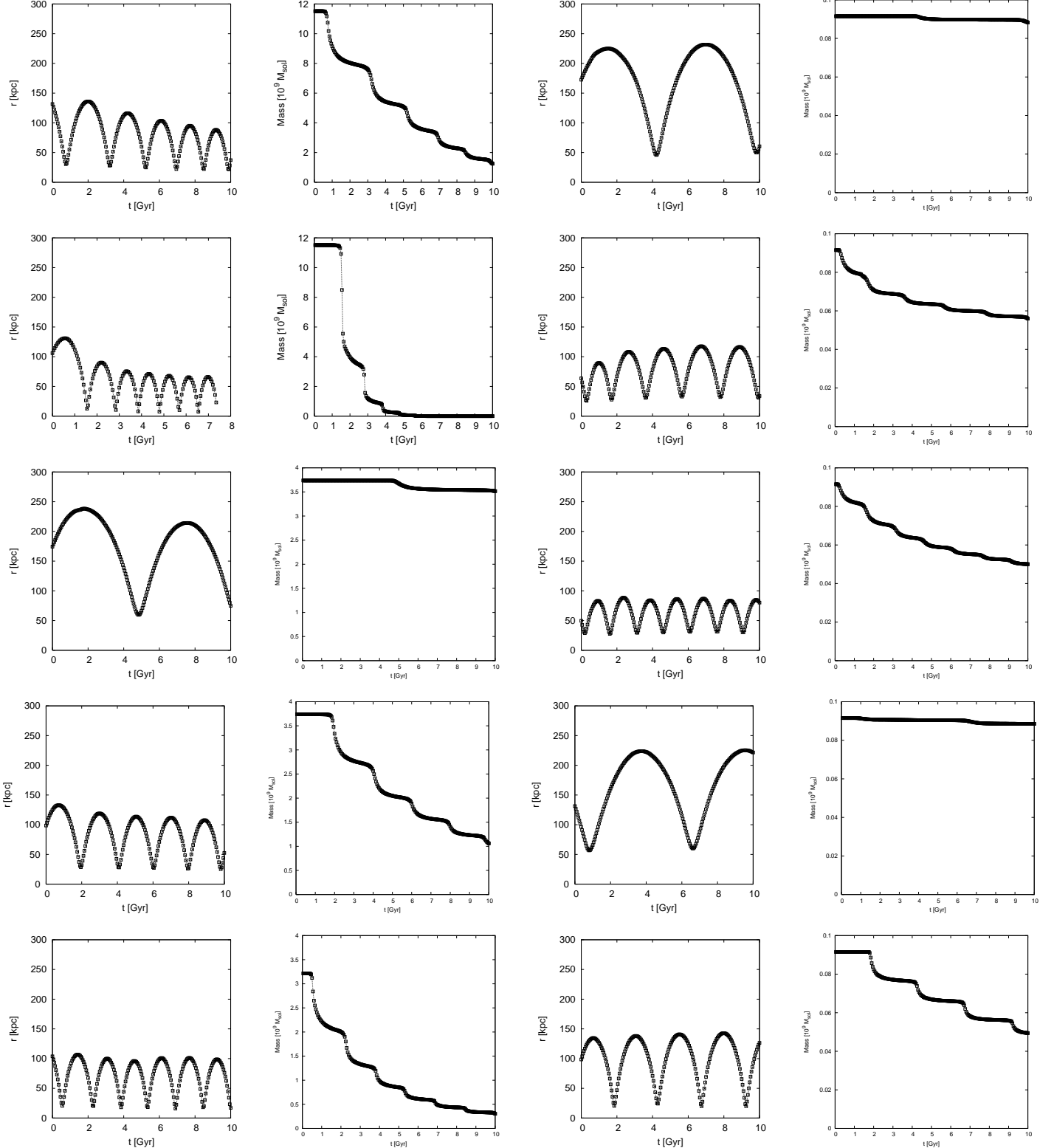


Fig. 9.— Decay and mass loss of individual satellites. The first two columns are for the five most massive satellites. The third and fourth ones are for five of the lightest satellites. First and third columns give the radius of the center of mass as a function of time. The figure demonstrates that dynamical friction does not play much of a role in evolution of the orbits.

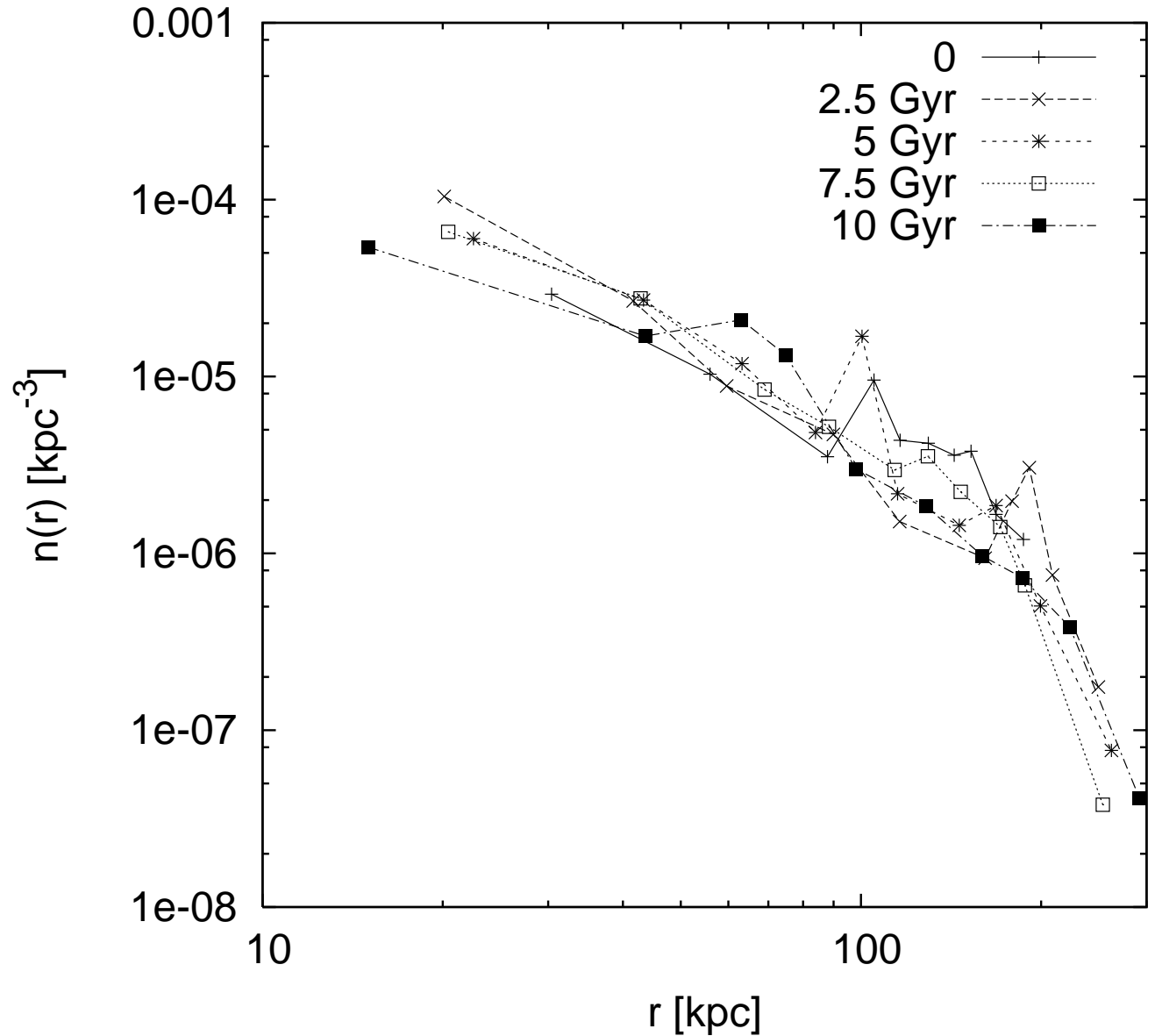


Fig. 10.— Evolution of the number density profile of satellites. The slope of the cusp remains constant over 10 Gyr..

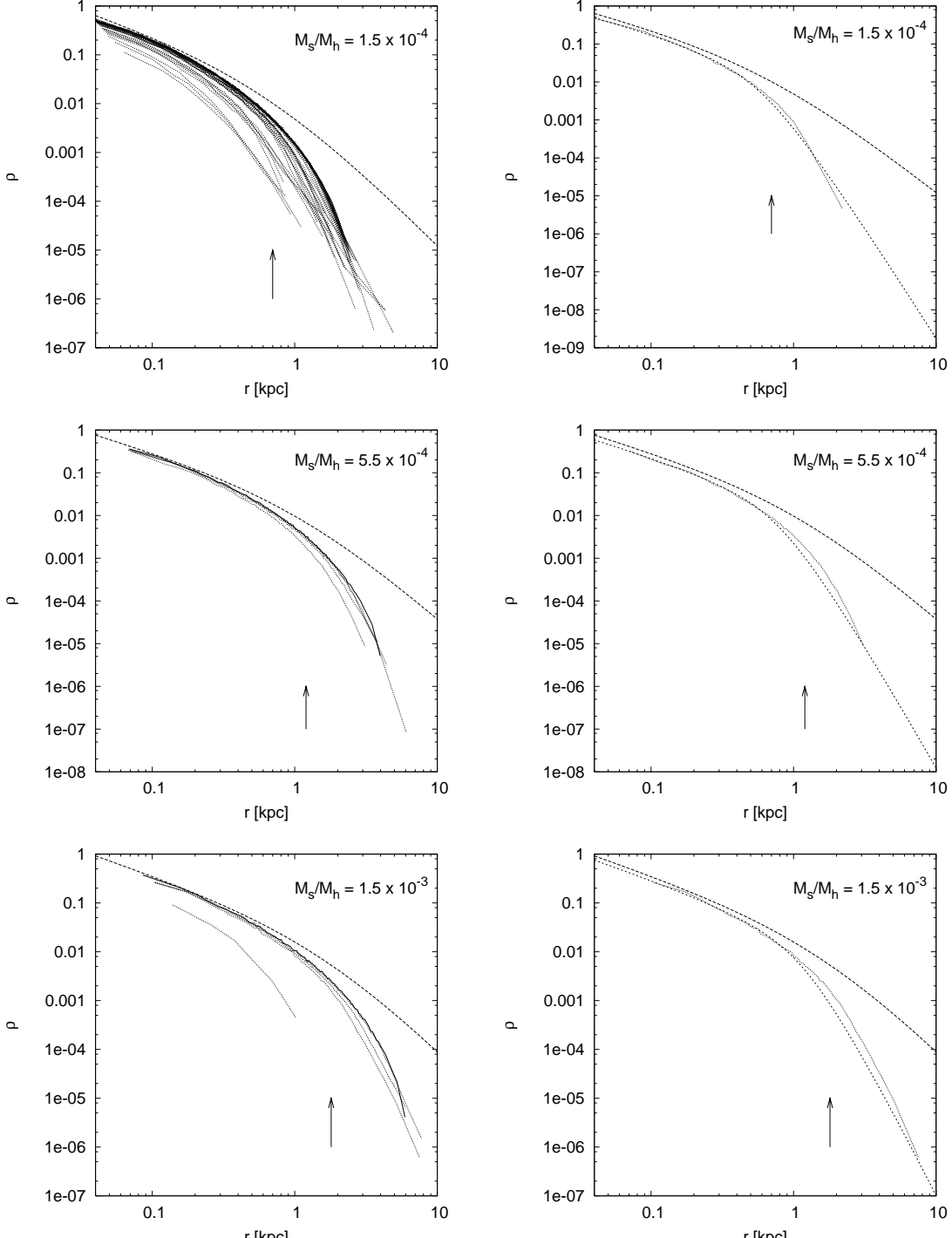


Fig. 11.— Density profiles for three different satellite mass bins at 10 Gyr. Top :  $M_{\text{sat}}/M_{\text{halo}} = 1.5 \times 10^{-4}$ , middle :  $M_{\text{sat}}/M_{\text{halo}} = 5.5 \times 10^{-4}$  and bottom  $M_{\text{sat}}/M_{\text{halo}} = 1.5 \times 10^{-3}$ . For the left plots, the thick line represents the unstripped density profile at the beginning of the simulation and the *dashed* line is the pure NFW model used to model the satellite. Arrows indicate the position of the scale radius  $r_s$ . Satellites are initially truncated so that  $r_{\text{edge}} \lesssim r_{\text{tidal}}$ . The right plots show the fit given by equation (8) for a typical profile of one of our satellites in each mass bin. The *short dashed* line is the best fit and the dotted line is the profile. As for the plots on the left, the *dashed* line is the pure NFW model.

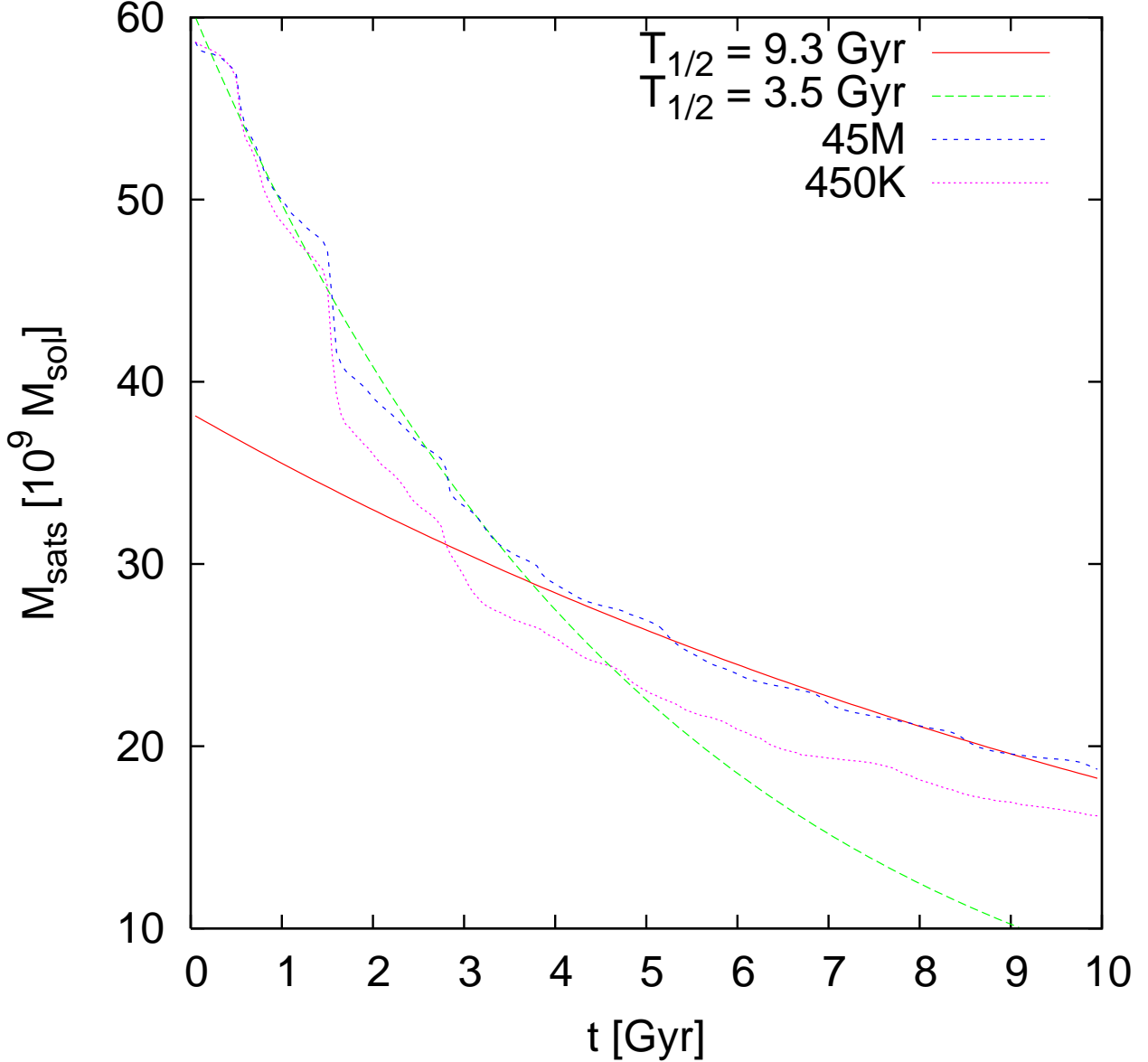


Fig. 12.— Evolution of the total mass bound in satellites as a function of time. The *short-dashed* and *dotted* lines are for the 45M and 450K simulation respectively. *Long-dashed* and *filled* lines are exponential decay fits to the 45M-particle run. The overall satellite decay is characterized by two distinct phases. The first one spans over the first 4 Gyr and corresponds to a very sharp mass loss with  $t_{1/2} = 3.5$  Gyr. For the second one, from 4 to 10 Gyr,  $t_{1/2} = 9.3$  Gyr.

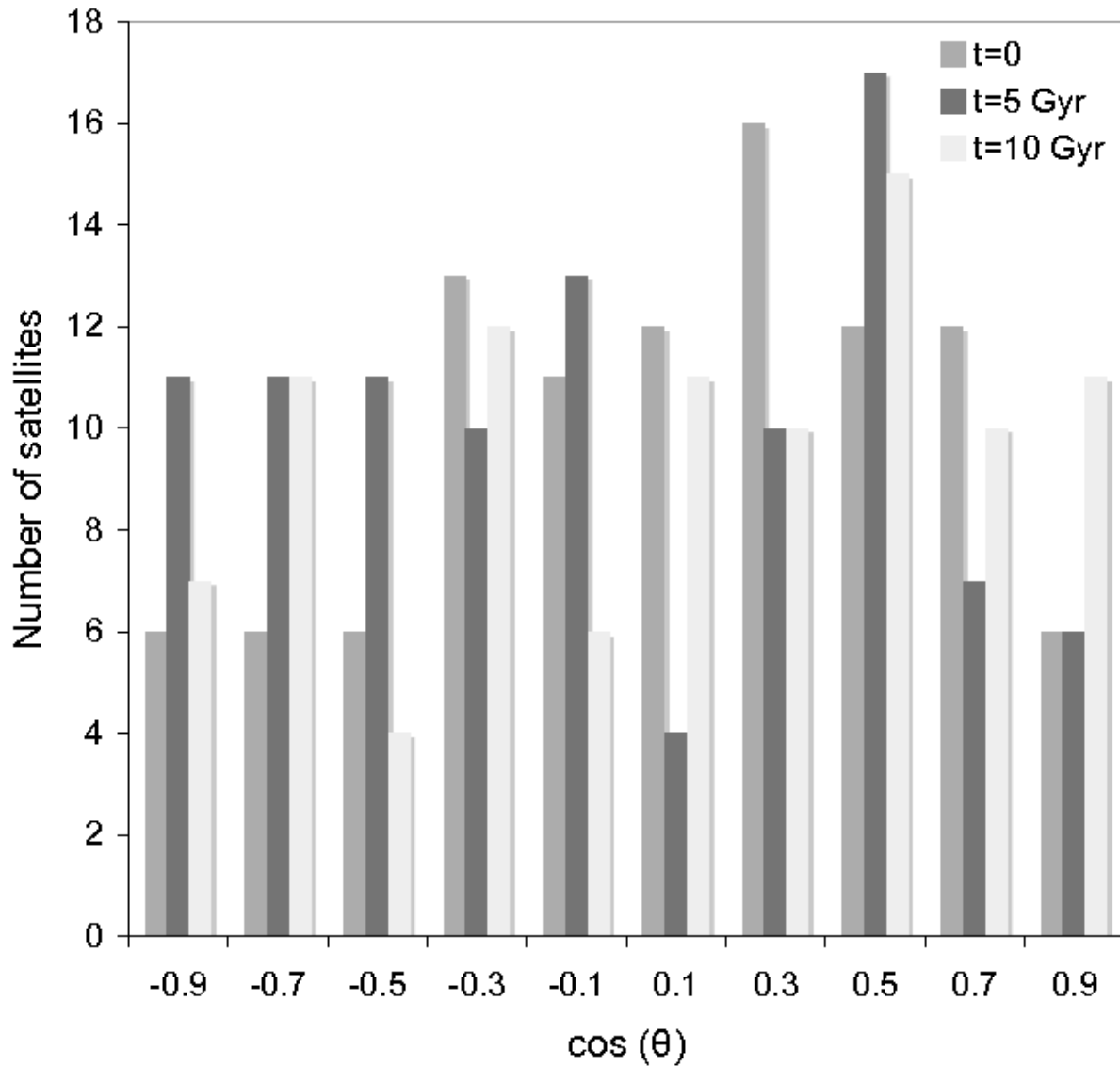


Fig. 13.— Number of satellites as a function of  $\cos(\theta)$ . Large fluctuations are initially present because of Poisson noise ( $\sqrt{10} = 3$ )

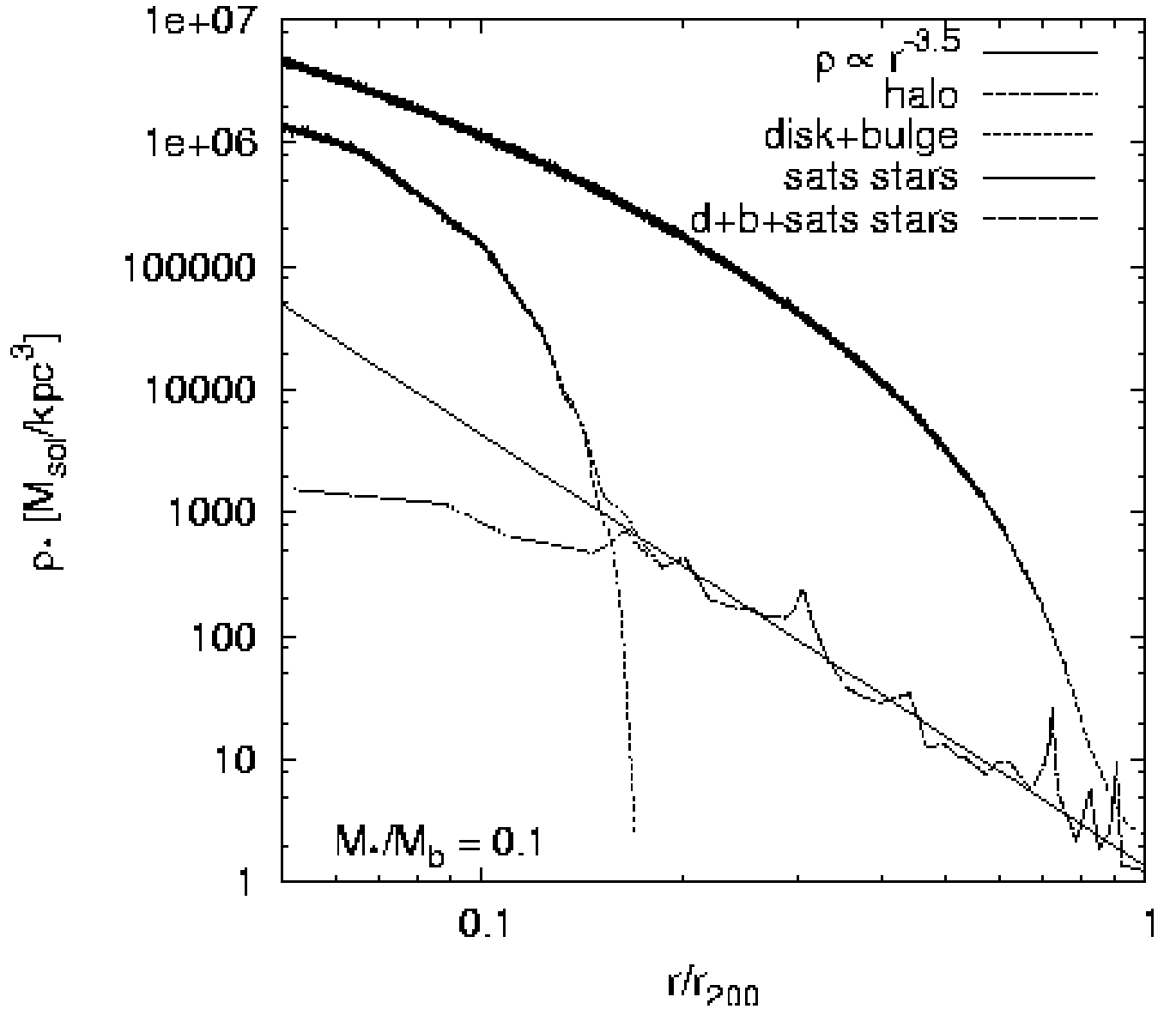


Fig. 14.— 3D density profile of the stripped stars plus stars still in satellites after 10 Gyr. We assume a constant star formation efficiency  $M_*/M_b=0.1$  and a baryon fraction of 0.171. The *long-dashed* line represents the dark halo density profile; *short-dashed* one the stellar component of the bulge+disk; the *dotted* line is associated with satellites star only and the *dash-dotted* line is the sum of the disk, bulge and satellites stellar component. For  $r/r_{200} > 0.2$ , the profile of satellites stars is well fitted by  $\rho \propto r^{-3.5}$ . The spikes in the satellite stellar component are associated with stars that are still bound to orbiting satellites.

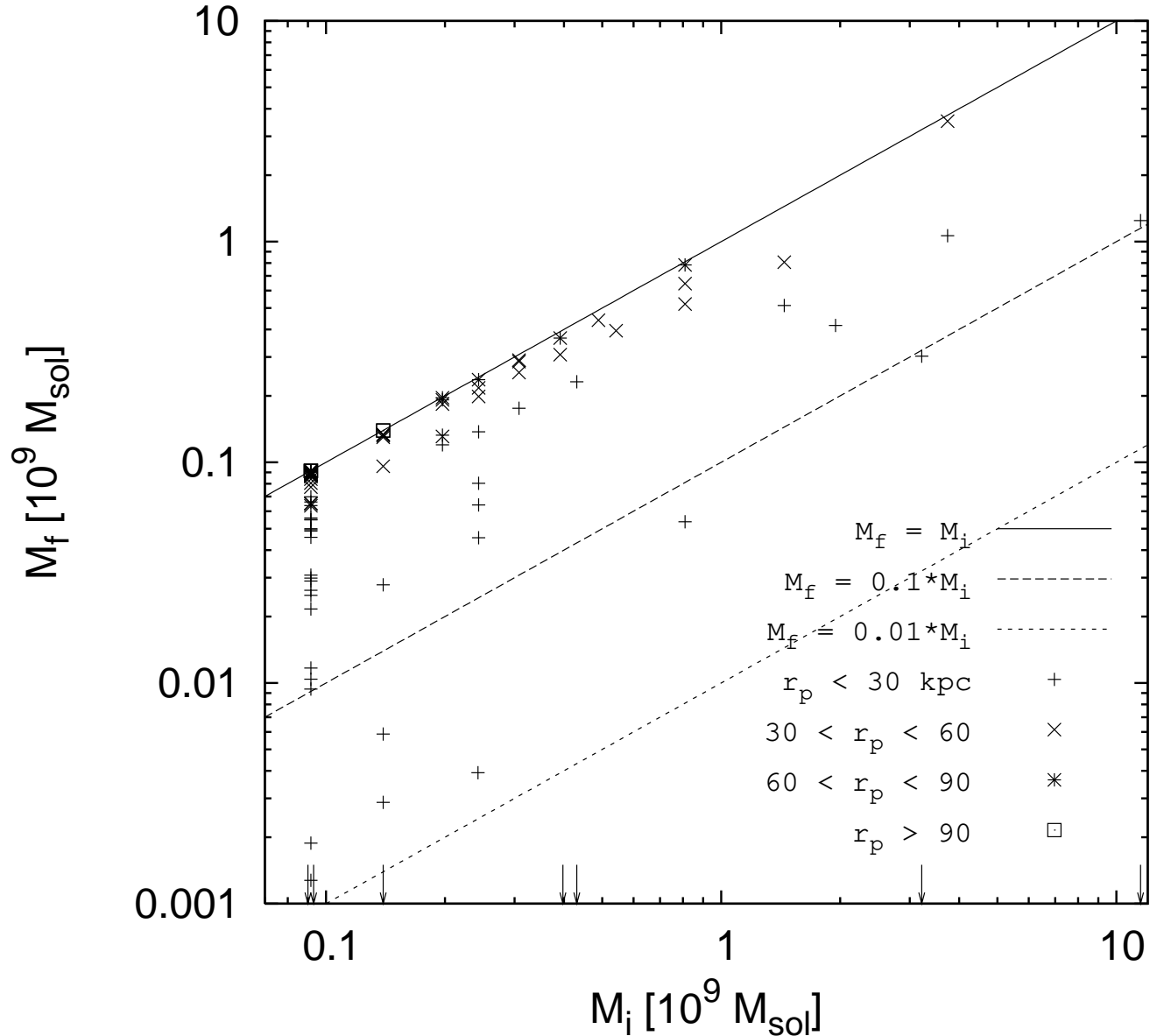


Fig. 15.— Scatter plot of the final mass  $m_f$  vs initial mass  $m_i$  for the 100 satellites in the experiment. Different symbols distinguish satellites according to pericenter. The arrows represent the seven satellites that are completely destroyed by the end of the simulation.

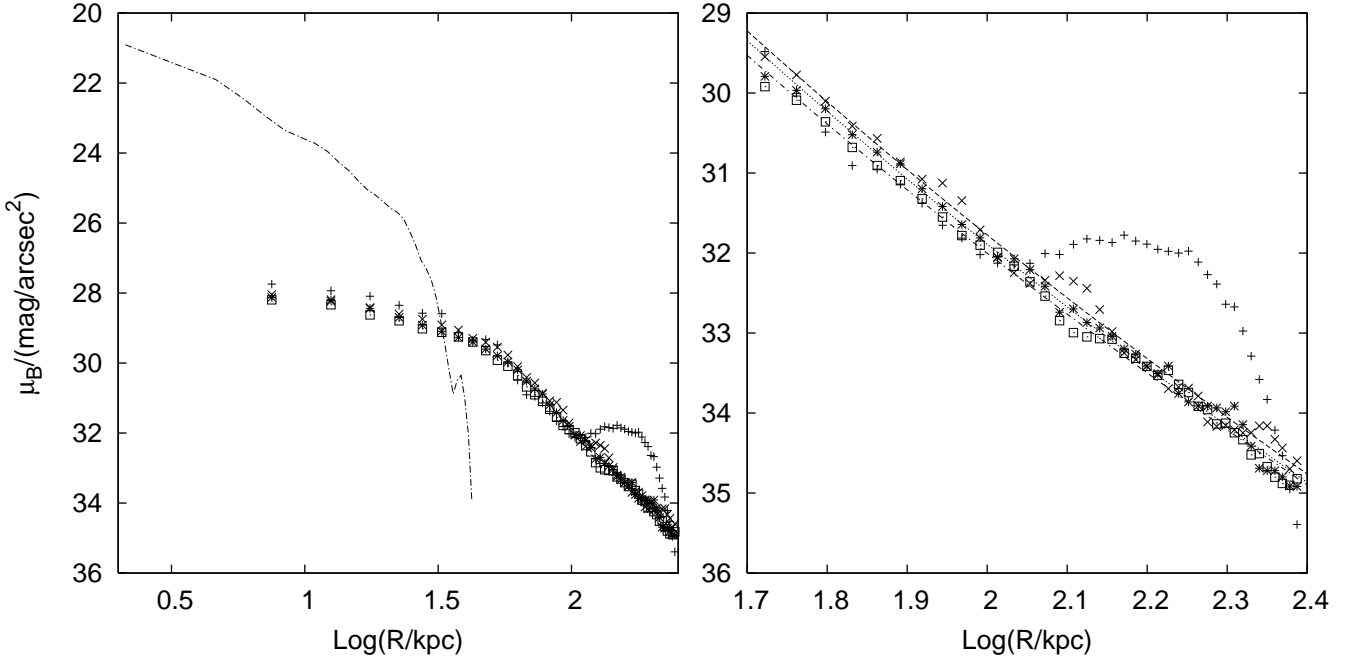


Fig. 16.— B-band surface brightness profiles of the stars tidally stripped from the satellites. The profiles are drawn assuming a star formation efficiency of 10% and a simple stellar population formed 1 Gyr prior to the beginning of the simulation. On both plots, the symbols are for four different snapshots : *plus* 2.5 Gyr, *X* 5.5 Gyr, *stars* 7.5 Gyr and *squares* 10 Gyr. On the left-hand side, the *dot-dashed* line shows the contribution of disk+bulge of M31 to the total surface brightness. On the right-hand side, a closeup shows straight lines corresponding to the best fit de Vaucouleurs profiles at 5, 7.5, and 10 Gyr. The feature around  $\log R = 2.2$  for the 2.5-Gyr snapshot is a consequence of the transient start and tends to disappear before 5 Gyr.

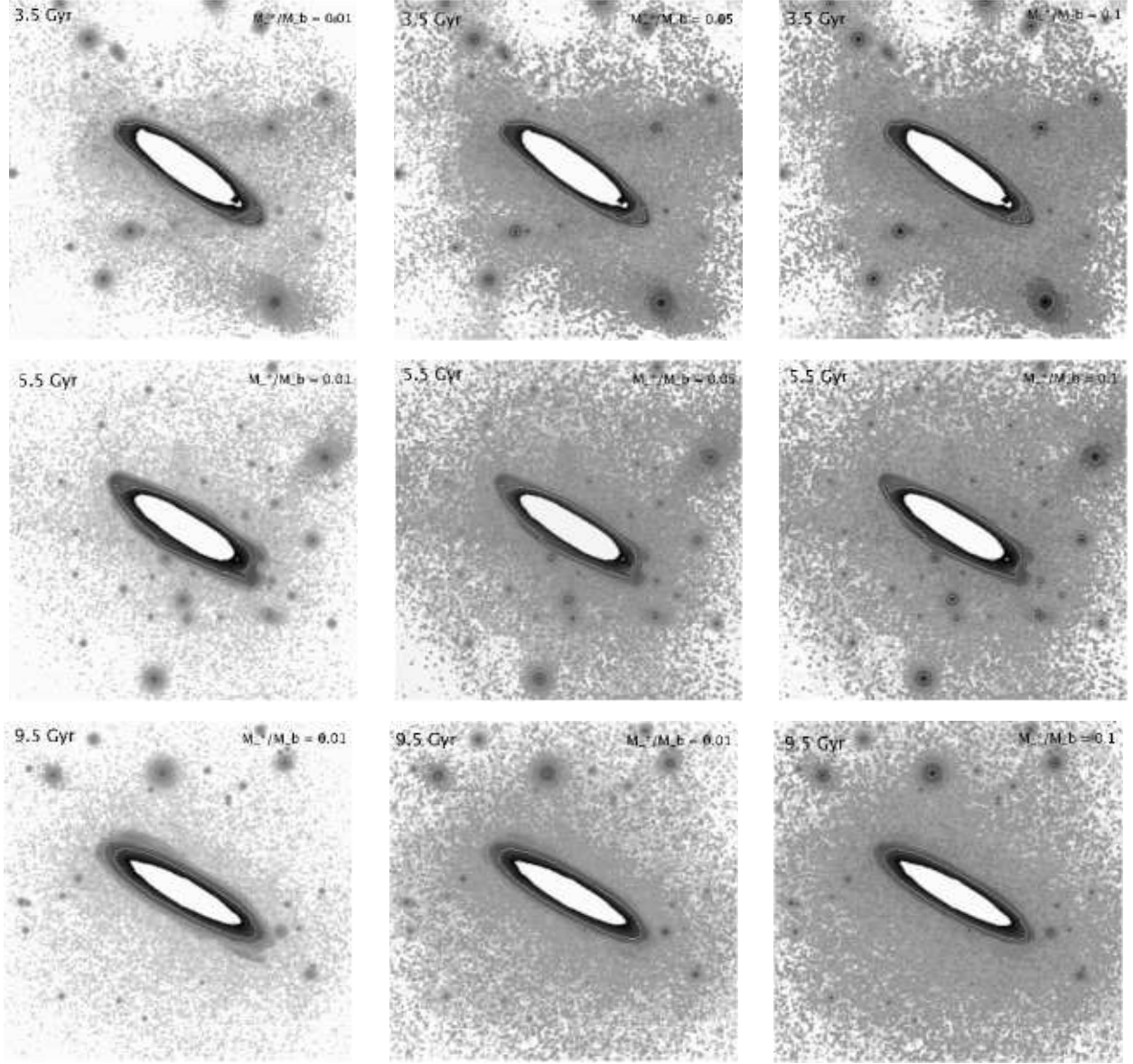


Fig. 17.— B-band CCD Photometric maps at  $2000 \times 2000$  pixel resolution showing a  $10^\circ \times 10^\circ$  field of the satellite stellar population taken from top to bottom 3.5, 5.5 and 9.5 Gyr. For each map, we assume a simple stellar population formed at  $t=-2.5$  Gyr. We show the contours corresponding to a surface brightness of 34.4, 31.9, 26.89, and 24.59 mag  $\text{arcsec}^{-2}$ . From one figure to another, we vary the star formation efficiency i.e. how much gas is converted into stars. *left column* :  $M_{\text{stars}}/M_{\text{baryons}} = 0.01$ , *middle* :  $M_{\text{stars}}/M_{\text{baryons}} = 0.05$  and *right column* :  $M_{\text{stars}}/M_{\text{baryons}} = 0.1$ . We assume a constant  $M_{\text{baryons}}/M_{\text{sat}} = 0.171$  for all satellites. The white patch in the center of M31 is to avoid saturation of the chip and corresponds to a limiting isophote of 24.59 mag  $\text{arcsec}^{-2}$ . (See high-resolution color version of these maps at <http://www.cita.utoronto.ca/~jgauthier/m31>)

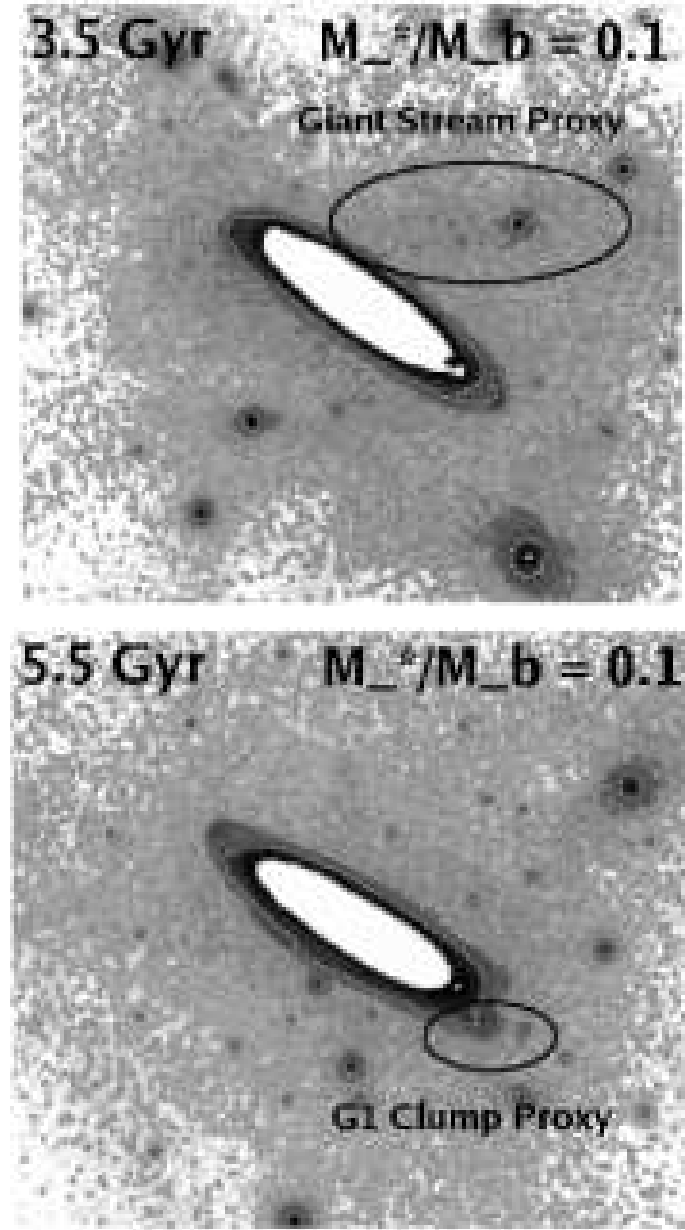


Fig. 18.— Close-up version of two Figure 17 maps showing features resembling both morphologically and photometrically to the Giant Stream and G1 Clump observed around M31. The surface brightness of our Giant Stream is about 28.5 mag arcsec<sup>-2</sup> in the B-band. (See *high-resolution color version of these maps at <http://www.cita.utoronto.ca/~jgauthier/m31>*)